Data-driven High-Frequency Mass Change Models from GRACE Ranging Residuals

Preprint manuscript (version 2) currently under review in *Journal of Geodesy (Springer Nature)* since September 23rd 2026 (submitted on August 17th 2026).

M. Cuadrat-Grzybowski[1*], F. Jacobs[1], P. N. A. M. Visser[1], J. G. de Teixeira da Encarnação[1]

[1*]Space Engineering, Astrodynamics and Space Missions Section, Delft University of Technology, Kluyverweg 1, Delft, 2629 HS, The Netherlands.

*Corresponding author(s). E-mail(s): M.Cuadrat-Grzybowski-1@tudelft.nl;
Contributing authors: F.Jacobs@tudelft.nl; p.n.a.m.visser@tudelft.nl; j.g.teixeiradaencarnacao@tudelft.nl;

Abstract

We present a fully data-driven framework for deriving 5-day surface mass change variations from GRACE residual Ka-band ranging (KBR) observations. The methodology establishes, for the first time, a spatially varying empirical transformation between observation-domain KBR observables—Line-of-Sight Gravity Differences (LGDs) and residual inter-satellite range—and Equivalent Water Height (EWH). Monthly geo-fits, representing the monthly gravity-field signal, are combined with 5-day post-fit residuals that capture sub-monthly variability. A hybrid observable formulation combining LGD and residual range information further reduces the observable-to-EWH regression errors associated with the individual formulations. Unlike existing approaches, the method operates entirely within the conventional GRACE Level-1B to Level-2 processing chain and does not require regularisation, Kalman filtering, or other geophysical external priors. An accompanying uncertainty propagation framework provides spatially and temporally resolved uncertainty estimates for all 5-day solutions, supporting their potential use in downstream geophysical and data-assimilation applications. Relative to the standard monthly products, the additional uncertainty

remains moderate, increasing by approximately 13–20% over land and 8–12% over the oceans, substantially below the ∼145% increase expected from an unconstrained reduction of the temporal averaging window. The recovered sub-monthly signals are validated through independent comparisons with ITSG-Grace2018 daily solutions and are further demonstrated using the 2007 Bangladesh floods and the January 2013 Cyclone Oswald event. The proposed framework provides a practical pathway for routinely generating uncertainty-aware high-frequency GRACE(-FO) mass change products from standard processing outputs.

Keywords: GRACE KBR, Post-fit residuals, Line-of-Sight Gravity Differences (LGD), Empirical model, Equivalent Water Height (EWH), Sub-monthly mass variations

1 Introduction

The Gravity Recovery and Climate Experiment (GRACE) and its successor GRACE Follow-On (GRACE-FO) have provided an unprecedented record of Earth's time-variable gravity field, allowing mass redistribution to be monitored at monthly to decadal scales (Wahr 2015; Frappart et al. 2016; Ramillien et al. 2016). Traditionally, GRACE gravity field models are released as Level-2 products, expressed either in spherical harmonic (SH) coefficients (e.g., Lemoine et al. 2007; Jäggi et al. 2022; Ince et al. 2019) or in "mascon" representations (Wiese et al. 2016; Save et al. 2016). These monthly solutions have become the standard for studying long-term changes in terrestrial water storage, ice mass, and ocean dynamics (Schmidt et al. 2008; Wouters et al. 2019; Schindelegger et al. 2021; Xiong et al. 2024).

While monthly gravity field solutions provide robust estimates of large-scale mass variability, their temporal resolution is fundamentally limited by the GRACE(-FO) orbital geometry and standard processing strategy. To overcome this limitation, several studies have developed higher temporal resolution products—most notably the ITSG-Grace2018 daily solutions from TU Graz (Mayer-Gürr et al. 2018), as well as other high-frequency releases (Lemoine and Bourgogne 2020; Ramillien et al. 2020; Rateb et al. 2024). The ITSG-Grace2018 daily solutions are typically truncated to spherical harmonic degree 40 (∼500 km half wavelength), reflecting the limited spatial sampling imposed by the GRACE orbit geometry and the need to stabilise the inversion. Such short-interval gravity fields generally rely on temporal regularisation or filtering, such as autoregressive (AR) schemes, to mitigate the ill-posed nature of the inversion (e.g., Kurtenbach et al. 2012; Kvas et al. 2019). Consequently, their nominal sampling interval (e.g., one day) does not reflect true temporal independence: the effective temporal decorrelation often spans two or more days, depending on the strength of the applied regularisation and the noise characteristics. Moreover, high-frequency GRACE solutions often incorporate additional spatial constraints derived from hydrological model statistics (Kvas et al. 2019), which are applied to stabilise the inversion and mitigate the limited information content due to orbital coverage. Recent studies have also explored retrieving high-frequency mass variations, at regional scales, from GRACE and GRACE-FO along-track observations without Kalman-type smoothing

(e.g., Li et al. 2024, 2025b,c). In such approaches, the gravity field is typically represented using a combination of spatio-temporal basis functions: Slepian functions in space (regionally restricted) and B-splines in time, with Tikhonov regularisation applied to ensure stable recovery. Nevertheless, reconstructing sub-monthly variability remains challenging due to the inherent trade-off between spatial and temporal resolution, which continues to constrain high-frequency gravity field modelling.

Furthermore, uncertainty quantification remains a major challenge, particularly in data assimilation frameworks of GRACE(-FO) data for hydrological applications, where quantifying errors is a key aspect (Yang et al. 2025; Wu et al. 2022; Retegui-Schiettekatte et al. 2025). Recent GRACE(-FO) data assimilation efforts, such as those implemented over the Ganges–Brahmaputra basin using ITSG-Grace2018 daily solutions (Gouweleeuw et al. 2018; Wu et al. 2022; Retegui-Schiettekatte et al. 2025), have highlighted the potential of high-frequency mass change models for improving short-term water storage estimates. Ideally, data assimilation systems would make use of the full error covariance structure of the GRACE(-FO) gravity field solutions (Yang et al. 2025). However, such covariance information is typically not distributed with the products, is difficult to independently reconstruct (Zhang et al. 2024), and often lacks transparency regarding the underlying assumptions. Additionally, application-ready uncertainty grids for end-users are generally not provided, especially at sub-monthly resolution, adding further challenges in the direct usability of high-frequency gravity solutions for hydrological or regional studies. Consequently, practical uncertainty estimations typically rely on empirical or analytical approximation methods (Boergens 2021; Boergens et al. 2022). For example, the Global Gravity-based Groundwater Product (G3P) project (Güntner et al. 2024) employs empirically modelled uncertainty estimates for monthly GRACE grids (Boergens et al. 2022), which, when compared with uncertainties propagated from full covariance matrices, tend to be conservative in magnitude and exhibit only moderate spatial correlations, typically below 0.75 when aggregated over major hydrological river basins (Boergens et al. 2022). This highlights the challenge of providing accurate, user-friendly uncertainty information for (sub-)monthly geophysical applications.

An alternative strategy is to bypass the (sub-)monthly (constrained) inversion processes entirely and work directly with Level-1B (Case et al. 2010) residual observations. In this context, *pre-fit residuals* are defined as the differences between the observed K-band range-rate measurements and their a priori simulated counterparts derived from background models, while *post-fit residuals* correspond to the pre-fit residuals after subtraction of the best-fitting monthly spherical harmonic gravity field solution. Recent studies have demonstrated that both pre-fit and post-fit residuals retain geophysical information that is otherwise filtered out during conventional monthly gravity field processing (Han et al. 2010, 2021b,a; Peidou et al. 2022; Ghobadi-Far et al. 2022). Exploratory analyses of residual Line-of-Sight Gravity Differences (LGDs) have shown that these quantities capture coherent sub-monthly signals, enabling the detection of rapid mass variations associated with transient phenomena (Cuadrat-Grzybowski et al. 2025) such as tropical cyclones and oceanic redistributions (Ghobadi-Far et al. 2022), floods (Han et al. 2021b,a), and even tsunamis induced by major earthquakes (Ghobadi-Far et al. 2020). These along-track LGD analyses demonstrate remarkable

potential for detecting "instantaneous" mass anomalies directly from GRACE measurements. However, their sensitivity remains constrained by the satellite ground-track geometry, which governs whether a given event is observed. Furthermore, these residuals are typically expressed in nm/s^2, which complicates direct interpretation in terms of geophysically meaningful units such as Equivalent Water Height, EWH (cm) or mass (Gt). Only a few studies have attempted simple transformations from residual range accelerations to mass anomalies, either using point-mass peak sensitivity (Spero 2021) or aggregated basin-level analyses (Zhu et al. 2025). However, these approaches are limited, as they typically assume analytical relations, a linear dependency, neglect side-lobe effects, and treat residual range accelerations as a direct proxy for LGDs without accounting for the residual centrifugal acceleration term (Ghobadi-Far et al. 2018).

Collectively, limited temporal independence, reliance on regularisation or external constraints, restricted ground-track coverage, and difficulties in translating orbital residuals to meaningful mass anomalies, highlight the challenges in accurately reconstructing sub-monthly gravity variations. To address these limitations, we propose a fully data-driven and GRACE-only framework that directly links GRACE K-band range (KBR)-based observations to gridded gravity field quantities, expressed in terms of EWH. The method exploits the information contained in the residual range-rate (post-fit) time series together with the corresponding monthly gridded EWH products. In contrast to existing high-frequency gravity field approaches that rely on temporal regularisation or external geophysical constraints (Kurtenbach et al. 2012; Kvas et al. 2019; Li et al. 2025b), the proposed framework introduces no additional priors, or regularisation assumptions. Instead, it leverages existing GRACE data products and processing pipelines, since post-fit residuals are routinely derived within monthly gravity field recovery. This involves spatially interpolating sub-weekly sets of these post-fit residuals and superimposing them onto the corresponding monthly spherical harmonic post-fits, which are referred to as *geo-fits*. This approach not only enables empirical reconstruction of sub-monthly gravity field variability at an enhanced spatio-temporal resolution but also allows for the direct estimation of gridded uncertainty grids suitable for end-user applications.

The paper is organised as follows: Sect. 2 describes the GRACE observations and Level-2 datasets used in this study, including the residual Level-1B observables, monthly and daily gravity-field solutions, and their transformation into EWH grids. Sect. 3 presents the proposed methodology, including the processing of residual Level-1B data, gridding of residual LGD and range observables, the altitude- and inter-satellite range correction, the observable-to-EWH transformation, and the hybridisation of KBR residual observables. Sect. 4 describes the uncertainty framework, including the individual uncertainty contributions associated with the observations, empirical corrections, transformation procedure, and monthly Level-2 uncertainty, as well as their combination into the final EWH uncertainty estimates. Sect. 5 presents the results and discussion, including the evaluation of the orbital configuration correction, the spatial characteristics of the observable-to-EWH transformation, validation of the 5-day EWH solutions against independent ITSG-Grace2018 daily solutions, uncertainty characterisation, and the temporal consistency analysis

of the derived solutions. Finally, Sect. 6 summarises the main findings and provides recommendations for future developments.

2 GRACE observations and Level-2 data processing

This section describes the GRACE observation products and processing steps used throughout this study. Section 2.1 introduces the residual Level-1B observables that form the basis of the proposed methodology. The monthly and daily Level-2 gravity field solutions used for regression, validation, and uncertainty estimation are then described in Sect. 2.2. Finally, Sect. 2.3 presents the processing of Level-2 spherical harmonic solutions into gridded EWH used throughout the remainder of the manuscript.

2.1 Residual Level-1B post-fit data

In this study, we utilise the CSR RL06 residual Level-1B (L1B) product (Bettadpur et al. 2025), an intermediate dataset linking the standard GRACE L1B observations and the monthly Level-2 (L2) gravity field solutions. The product contains both the pre-fit observables, obtained after reduction of the nominal L1B measurements by the background force and measurement models used in the L2 processing chain (Bettadpur 2018a), and the corresponding monthly post-fit residuals. Unlike conventional L2 products, the residual L1B dataset preserves the original high temporal resolution of the K-band ranging observations while maintaining consistency with the monthly gravity field solutions from which the residuals were estimated. This combination provides direct access to sub-monthly information contained in the KBR measurements and forms the basis of the methodology developed in this study.

The proposed methodology relies on two key variables inherited from CSR's range-rate processing strategy (Pini 2012; Bettadpur et al. 2025). Together, they provide a natural decomposition of the GRACE observations into the monthly gravity-field signal and the remaining sub-monthly variability:

- **Geo-fit**: The component of the fitted range-rate signal that is reconstructed exclusively from the estimated monthly SH gravity field coefficients. In practice, it may be written as $\mathbf{A}_{\mathrm{SH}}\hat{\mathbf{x}}_{\mathrm{SH}}$, where $\mathbf{A}_{\mathrm{SH}}$ denotes the observation sensitivity matrix derived from the GRACE inter-satellite geometry and $\hat{\mathbf{x}}_{\mathrm{SH}}$ the estimated SH coefficient vector.
- **Post-fit Residuals**: The difference between the pre-fit observations and the complete least-squares fit, containing sub-monthly variability, modelling errors, and measurement noise.

2.2 Level-2 solutions

2.2.1 Monthly solutions

We primarily use the CSR RL06 monthly SH gravity field solutions (up to degree and order 60), available via ICGEM (Ince et al. 2019), to derive the empirical transformation between KBR observables and equivalent water height. These solutions span the

full GRACE mission period from April 2002 to June 2017. In this framework, CSR's SH coefficients serve as the direct model representation of the updated residual Level-1B geo-fit (see Sect. 2.1). The static field GGM05C (Ries et al. 2016) provided by CSR is used to remove the long-term mean gravity field from the monthly SH solutions.

To estimate the uncertainty associated with the Level-2-derived EWH grids, we adopt the same ensemble-based uncertainty estimation methodology described in Cuadrat-Grzybowski et al. (2026a), using independently processed monthly gravity field solutions. In addition, the AOD1B uncertainty contribution is included following the approach implemented in version 5 of the DDK3-filtered (Kusche et al. 2009) TUD-L3-EWH_UNC product. The uncertainty estimation is adapted to the present framework, including the specific filtering and processing choices described in Sect. 2.3. The considered Level-2 solutions are summarised in Table 1, and all solutions are obtained from ICGEM (Ince et al. 2019).

Table 1 Monthly GRACE Level-2 gravity field solutions used for the EWH uncertainty estimation.

Processing centre	Solution	Reference
CSR	RL06	(Bettadpur 2018b)
JPL	RL06	(Yuan 2018)
GFZ	RL06	(Dahle et al. 2019)
TU Graz	ITSG-Grace2018	(Mayer-Gürr et al. 2018)
HUST	HUST-Grace2024	(Zhou et al. 2024)
APM & SYSU	APM-SYSU	(Ince et al. 2019)
Tongji	Tongji-Grace2022	(Chen et al. 2023)
COST-G	RL02.1	(Jäggi et al. 2022)

2.2.2 Daily Kalman-filtered solutions

For validation purposes, we use the ITSG-Grace2018 Kalman-filtered gravity field solutions from TU Graz (Kvas et al. 2019), provided at a daily rate as SH coefficients up to degree and order 40. Given their state-of-the-art temporal resolution, they are well-suited for assessing the sub-monthly mass change signals of the high-frequency solutions derived in this study.

2.3 From Level-2 to EWH grids

All Level-2 solutions described in Sect. 2.2.1 and Sect. 2.2.2 are first converted to equivalent water height grids via spherical harmonic synthesis using l3py software (Kvas 2018). Prior to this step, the static background field GGM05C (Ries et al. 2016) is removed to isolate the time-variable gravity signal.

The resulting residual spherical harmonic coefficients are filtered using decorrelation filters of the DDK family (e.g., DDK1–DDK5) (Kusche et al. 2009), which are designed to suppress correlated north–south stripes while preserving the large-scale geophysical signal. The choice of a DDK-type filter, particularly DDK3, is motivated by hydrological applications: it minimises amplitude damping and phase distortion of

the signal, thereby conserving the spatial distribution of the original mass variations. This ensures that the filtered grids retain spatial patterns closely resembling the unfiltered trend estimates of EWH grids derived from Level-2 solutions, and aligns with established practices validated against global hydrological models (e.g., Werth et al. 2009; Qian et al. 2022; Li et al. 2025a).

To reduce the dominance of long-wavelength (low-degree) signals which the residual LGD and range observables are less sensitive to, a gentle truncation is applied. The filter follows the smooth polynomial form of the low-pass function proposed by Barthelmes (n.d.) (accessed on 17 December 2025), but is inverted to obtain a high-pass equivalent that mimics the effective high-pass behaviour (approximately below 0.9 mHz) of the LGD time-series filtering (see Sect. 3.1). Each spherical harmonic degree l is thus down-weighted according to

$$w_{\mathrm{HP}}(l) = 1 - w_{\mathrm{LP}}(l), \tag{1}$$

where $w_{\mathrm{LP}}(l)$ are the low-pass filter coefficients defined as (Barthelmes n.d.)

$$w_{\mathrm{LP}}(l) = \begin{cases} 1, & l \le l_a, \\ \left(\dfrac{l - l_a}{l_b - l_a}\right)^4 - 2\left(\dfrac{l - l_a}{l_b - l_a}\right)^2 + 1, & l_a < l < l_b, \\ 0, & l \ge l_b, \end{cases} \tag{2}$$

where $l_a = 2$, and l_b controls the smoothness of the transition between retained and attenuated degrees.

We performed a brief analysis (as described in App. A), and given input from literature (e.g., Werth et al. 2009; Qian et al. 2022; Li et al. 2025a), the combination of DDK3 and a gentle truncation with $l_b = 7$ was found to be most optimal.

3 Methodology

This section presents the proposed data-driven framework for deriving sub-monthly EWH grids from GRACE residual Level-1B observations. The methodology consists of five main steps. First, residual (KBR) range-rate observations are transformed into residual LGDs and residual range observables (Sect. 3.1). Second, the corresponding monthly geo-fits and sub-monthly post-fit residuals (obtained from step 1) are spatially gridded to obtain global high-frequency mass-anomaly proxies (Sect. 3.2). Third, because these observables depend on the instantaneous satellite altitude and inter-satellite range, an empirical correction is introduced to remove this orbital dependency (Sect. 3.3). Fourth, the corrected gridded observables are related to EWH through a spatially varying empirical transformation (Sect. 3.4). Finally, the LGD- and residual-range formulations are combined into a hybrid solution that exploits the superior spatial localisation of LGDs while mitigating their side-lobe artefacts using residual-range (Sect. 3.5). The resulting product consists of global sub-monthly EWH grids derived directly from residual Level-1B observations.

3.1 Residual Level-1B data processing

Residual LGDs and residual inter-satellite range both provide spatially and temporally localised information on mass anomalies, but with different frequency content. Owing to the differentiation involved in their derivation, residual LGDs emphasise more spatially localised gravity signals, whereas residual inter-satellite range exhibits a broader spatial response, with sensitivity to mass variations distributed over larger spatial scales as illustrated, for example, in Fig. 1 of Ray et al. (2009). Starting from the residual range-rate observations described in Sect. 2.1, both observables are derived through time-domain and frequency-domain processing.

The relationship between residual range acceleration and LGDs follows from the relative GRACE equation of motion in the Line-of-Sight (LoS) direction (Weigelt 2017; Ghobadi-Far et al. 2018):

$$\delta g_{AB}^{\mathrm{LoS}} = \delta\ddot{\rho} - \delta\left(\frac{1}{\rho}\left(\|\dot{\mathbf{x}}_{AB}\|^2 - \dot{\rho}^2\right)\right), \tag{3}$$

where $\delta g_{AB}^{\mathrm{LoS}}$ denotes the residual LGD between satellites A and B, ρ is the inter-satellite separation, $\dot{\rho}$ and $\ddot{\rho}$ are the range rate and range acceleration, respectively, and $\dot{\mathbf{x}}_{AB}$ is the relative velocity vector between satellites A and B. The first term on the right-hand side, $\delta\ddot{\rho}$, represents the residual range acceleration after background model removal, while the second term corresponds to the residual centrifugal contribution caused by the curvature of the orbital motion and the nominally horizontal orientation of the inter-satellite vector. For the sake of brevity, we will hereafter refer to $\delta g_{AB}^{\mathrm{LoS}}$ simply as $\delta g_{||}$ and to the residual centrifugal term as δg_{cf}.

The residual centrifugal term can be accounted for through the frequency-domain transfer function proposed by Ghobadi-Far et al. (2018), yielding the practical processing relation

$$\delta g_{||}(t) = \mathcal{F}^{-1}\{Z(f)G_{\mathrm{BP}}(f)\mathcal{F}\{\mathcal{D}\{\delta\dot{\rho}(t)\}\}\} + \Delta_{\mathrm{TF}}, \tag{4}$$

where f denotes the frequency, $\mathcal{F}\{\cdot\}$ represents the Fourier transform, $G_{\mathrm{BP}}(f)$ is the gain of the fourth-order Butterworth band-pass filter with a frequency range of 0.9–11 mHz (Ghobadi-Far et al. 2018; Peidou et al. 2022), $\mathcal{D}\{\cdot\}$ denotes the numerical time derivative (approximated by a fourth-order central finite difference), $Z(f)$ is the transfer function approximating the effects of the residual centrifugal acceleration term, and Δ_{TF} is the error associated to the use of $Z(f)$. For further details regarding this pre-processing step and the residuals used (Bettadpur et al. 2025), we refer the reader to Cuadrat-Grzybowski et al. (2025). Lastly, the residual inter-satellite range, denoted by $\delta\rho$, is obtained from the residual range rates by applying the same band-pass filter followed by cumulative trapezoidal integration in the time domain.

3.2 Residual LGD and range gridding

The empirical framework relies directly on the GRACE post-fit residuals and their corresponding geo-fits, which are the estimated monthly SH coefficients in the post-fit

domain (see Sect. 2). These geo-fits represent the monthly gravity field expressed as LGDs or range-equivalent KBR quantities at the observation times and positions of the GRACE satellites. An overview of the processing procedure from residual post-fit time series to grids can be found in Fig. 1, which is explained in the following sections.

3.2.1 Geo-fit gridding

We first define the 5-second geo-fit (Sect. 2.1) time series as $K(t)$, obtained from the monthly SH solutions in the observation domain as residual LGD or range-equivalent quantities along the GRACE orbit. To obtain the monthly grid, the geo-fit time series are mapped to a spatial grid through a gridding operator $\mathcal{G}_{\text{geo}}$,

$$\hat{K}(\lambda, \phi) = \mathcal{G}_{\text{geo}}\{K(t)\}, \tag{5}$$

which consists of a monthly median aggregation on a coarse grid followed by spatial interpolation,

$$\mathcal{G}_{\text{geo}} = \mathcal{I}_{0.5^\circ} \circ \mathcal{M}_{2^\circ}, \tag{6}$$

where $\mathcal{M}_{2^\circ}$ denotes the median of all samples falling within each $2^\circ \times 2^\circ$ grid cell over one month, and $\mathcal{I}_{0.5^\circ}$ denotes the interpolation of this coarse grid onto a $0.5^\circ \times 0.5^\circ$ regular mesh.

In practice, the operator $\mathcal{M}_{2^\circ}$ is applied by aggregating the 5-second geo-fit time series over each month onto a coarse $2^\circ \times 2^\circ$ grid (Fig. 1a, middle panel). Within each grid cell, the median of all available samples is taken, consistent with the assumption that monthly geo-fits contain no sub-monthly geophysical variability. This aggregation provides a spatial representation of the monthly grid while mitigating along-track artefacts originating from residual accelerometer biases and imperfections in the estimated initial state vector. These effects are inherent to the inversion process and, although largely minimised through CSR's robust parametrisation strategy (Pini 2012), can locally persist in the post-fit domain (see along-orbit artefact east of the Amazon river basin in Fig. 1a, left panel).

Subsequently, the operator $\mathcal{I}_{0.5^\circ}$ interpolates the coarse grid onto a finer $0.5^\circ \times 0.5^\circ$ mesh (Fig. 1a, right panel). This target resolution is motivated by the along-track sampling of the GRACE satellites: with a mean orbital velocity of ~ 7.7 km/s and a 5 s sampling interval, the minimum spatial separation between consecutive measurements is approximately 38.5 km, corresponding to $\sim 0.35^\circ$ at the equator. A slightly coarser 0.5° grid is therefore adopted. This refinement (*regridding*) was tested through forward simulations using monthly L2 SH solutions, confirming that the associated power loss remains below the instrument noise level for most months and that the essential spatial characteristics of the gravity field are preserved (not shown).

3.2.2 Spatial interpolation and combination of post-fit residuals

The post-fit residuals, denoted as $\delta K(t)$, represent sub-monthly variations with respect to the monthly geo-fit baseline. These are provided as along-track range and LGD time series.

To obtain residual grids, a gridding operator $\mathcal{G}_{\text{res}}$ is defined for consecutive 5-day intervals t_k,

$$\delta\hat{K}^{5\text{d}}(t_k, \lambda, \phi) = \mathcal{G}_{\text{res}}\{\delta K(t)\}_{t_k}, \tag{7}$$

with

$$\mathcal{G}_{\text{res}} = \mathcal{I}_{0.5^\circ} \circ \mathcal{T}_{5d}, \tag{8}$$

where $\mathcal{T}_{5d}$ partitions the time series into 5-day subsets, and $\mathcal{I}_{0.5^\circ}$ denotes spatial interpolation onto the $0.5^\circ \times 0.5^\circ$ grid.

This 5-day interval is chosen following Rateb et al. (2024); Sun et al. (2024), who demonstrated that 5-day GRACE solutions (CSR) provide sub-monthly hydrological information while maintaining sufficient ground-track coverage of approximately 250 km (except for months with unfavourable near-repeat ground track patterns). Each subset is then mapped onto the regular grid via $\mathcal{I}_{0.5^\circ}$ using 2D Delaunay triangulation. This ensures spatial consistency with the geo-fit grids while preserving the sub-monthly variability captured by the residuals.

To mitigate artefacts arising from gaps in ground-track coverage, manifesting as sharp edge structures or discontinuities in the interpolated grids (Fig. 1b), a spatial Gaussian smoothing is subsequently applied to the residual grids. The smoothing employs a Gaussian kernel width of 8.75° and primarily suppresses edge artefacts without removing geophysically meaningful signals (internal sensitivity not shown).

Finally, the 5-day residual grids are combined with the monthly geo-fit grid to form the high-frequency geo-fit product,

$$\hat{K}^{5\text{d}}(t_k, \lambda, \phi) = \hat{K}(t_k, \lambda, \phi) + \delta\hat{K}^{5\text{d}}(t_k, \lambda, \phi), \tag{9}$$

yielding temporally enhanced 5-day LGD and range grids. These grids form the input for the subsequent hybrid transformation to EWH described in Sect. 3.5.

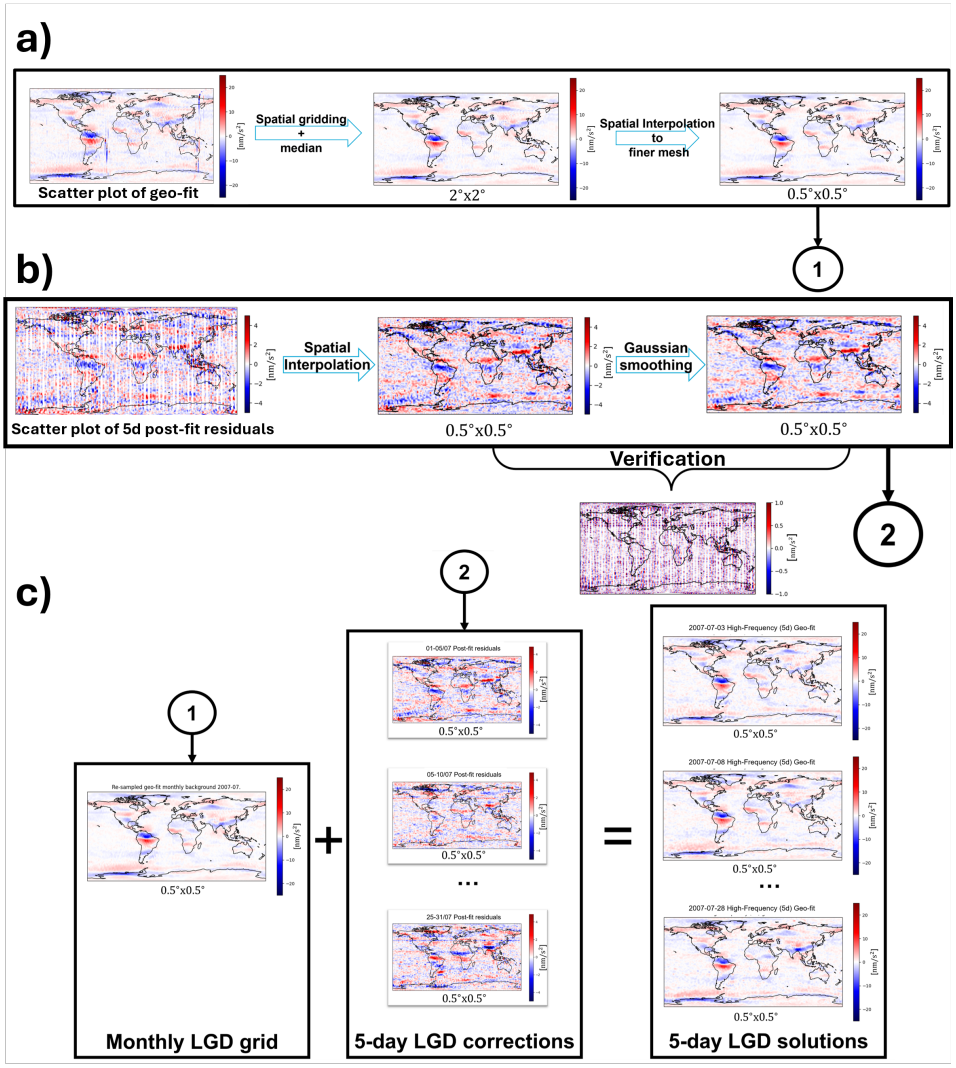


Fig. 1 Schematic overview of the GRACE residual gridding procedure for LGDs. (**a**) Monthly geo-fit residuals are aggregated onto a $2° \times 2°$ grid and then refined to a $0.5° \times 0.5°$ target grid. (**b**) Post-fit residuals are grouped into 5-day subsets and interpolated onto the $0.5° \times 0.5°$ grid with Gaussian smoothing for the removal of sharp discontinuities. (**c**) The 5-day residual grids are combined with the monthly geo-fit grid, yielding 5-day high-frequency geo-fit grids.

3.3 Altitude and inter-satellite range correction

The gridded LGD and residual-range grids obtained in the previous section represent observation-domain proxies of mass anomalies rather than geophysical quantities directly. Although they localise the underlying mass variations, their amplitudes remain dependent on the instantaneous GRACE orbital configuration, primarily

through variations in the mean satellite altitude and inter-satellite separation. Consequently, identical mass anomalies observed under different orbital geometries do not produce identical observable amplitudes. Before establishing an empirical relationship with EWH grids, these geometry-dependent effects must therefore be corrected.

3.3.1 Power-law representation of orbital geometry effects

We introduce an empirical correction that accounts for variations in the inter-satellite range ρ and mean satellite altitude $\bar{h}$ (or equivalently, circular orbital radius $\bar{r}$). We begin with a general separable power-law formulation relating the observable to a reference orbital configuration:

$$\frac{K_{\mathrm{ref}}(t)}{K(t)} \approx \left(\frac{\bar{r}(t)}{\bar{r}_{\mathrm{ref}}(t)}\right)^{n_r} \left(\frac{\rho(t)}{\rho_{\mathrm{ref}}(t)}\right)^{n_L}, \tag{10}$$

where $K(t)$ denotes the considered KBR observable (LGD or residual range) time-series, and the subscript "ref" refers to a reference orbital configuration (defined in Sect. 3.3.3). The exponents n_r and n_L describe the sensitivity to orbital radius and inter-satellite range, respectively. The formulation assumes that the amplitude variations introduced by orbital geometry can be separated into contributions from the mean orbital radius and the inter-satellite separation.

The range dependency in Eq. 10 is motivated from the first-order behaviour of the gravity difference between the two GRACE satellites. For a GRACE-type configuration, the two satellites follow nearly identical orbits, such that $\|\boldsymbol{r}_A\| \approx \|\boldsymbol{r}_B\| \approx \bar{r}$. Therefore, the gravity difference is dominated by the along-track (LoS) direction (denoted as x):

$$g_{AB} = g(\boldsymbol{r}_B) - g(\boldsymbol{r}_A) \approx \left(\frac{\partial g}{\partial x}\right) \rho, \tag{11}$$

where $\rho = \|\boldsymbol{r}_B - \boldsymbol{r}_A\|$ is the inter-satellite range and $\partial g/\partial x$ represents the gravitational acceleration gradient along the line-of-sight direction. Since gravitational acceleration gradients decay approximately as a power law with orbital radius inherited from the spherical harmonic representation of the Earth's gravitational field, we represent this behaviour by $\partial g/\partial x \propto (R/\bar{r})^{n_r}$, where R is the Earth's mean reference radius and n_r is the *effective* orbital radius exponent. Furthermore, the first-order approximation indicates indicates a linear dependency of the gravity difference on the satellite separation, motivating $n_L = -1$ in Eq. 10. This dependency is further assessed using controlled orbital simulations with both LGD and residual-range observables, yielding $n_L \approx -1$ with a standard deviation of approximately 0.003 (not shown). Given the consistency across observables and the limited variability, we fix $n_L = -1$.

3.3.2 Parameter estimation

Using the previously established range dependency, the range contribution can be removed explicitly by normalising the observable by ρ, resulting in

$$\frac{K_{\mathrm{ref}}/\rho_{\mathrm{ref}}}{K/\rho} \approx \left(\frac{\bar{r}}{\bar{r}_{\mathrm{ref}}}\right)^{n_r}. \tag{12}$$

The correction is therefore reduced to the estimation of the parameter n_r. Taking the natural logarithm transforms Eq. 12 into a linear relationship:

$$\ln\left(\frac{K_{\mathrm{ref}}/\rho_{\mathrm{ref}}}{K/\rho}\right) = n_r \ln\left(\frac{\bar{r}}{\bar{r}_{\mathrm{ref}}}\right). \tag{13}$$

This formulation corresponds to a one-parameter linear regression problem:

$$y = n_r x_h. \tag{14}$$

The standard least-squares solution was found to be sensitive to outliers caused by the large range of simulated orbital configurations. Therefore, the estimation is performed using a weighted least-squares approach with Tukey's bisquare weighting function. The residual scale is estimated as the robust standard deviation (σ_r) computed from the median absolute deviation, with the tuning constant c varied between 0.5 and 3.5 to assess sensitivity to outlier down-weighting. Residuals exceeding $c\,\sigma_r$ are assigned zero weight, while smaller residuals are progressively down-weighted according to the Tukey bisquare function.

3.3.3 Simulation setup

The orbital radius exponent n_r is estimated from an ensemble of controlled orbital simulations designed to represent the range of orbital configurations encountered throughout the GRACE mission. Simulations are generated around a nominal reference orbit (Case 0), defined by a mean altitude of $\bar{h}_0 = 450$ km and an inter-satellite range of $\rho_0 = 220$ km. Perturbations in the initial mean altitude and inter-satellite range ($\Delta\bar{h}_0, \Delta\rho_0$) are introduced as listed in Table 2. These configurations span conditions ranging from the early mission phase, with altitudes above 500 km, to the end-of-mission phase, at approximately 300 km, while also sampling substantial variations in inter-satellite separation.

Table 2 Initial simulation conditions for the GRACE satellite pair, including the mean orbital altitude and inter-satellite range.

Case	0	1	2	3	4	5	6	7	8	9	10
Δh_0 [km]	0	+250	-250	0	0	-250	+250	-125	+125	0	0
$\Delta\rho_0$ [km]	0	0	0	+120	-120	-120	+120	0	0	-60	+60

The orbit propagation is performed using the open-source *Tudatpy* software (Dirkx et al. 2022). A Cowell formulation with a Runge–Kutta–Fehlberg 7(8) integrator is used, with a fixed step size of 5 s and a simulation duration of 30 days. The force model includes only gravitational accelerations. The static gravity contribution is removed using the GGM05C model, while a set of randomly selected monthly CSR RL06 solutions spanning the majority of the GRACE mission lifetime (Table 3) is used to introduce realistic temporal gravity variations.

Table 3 Selected CSR RL06 monthly GRACE solutions used for the estimation of the orbital radius exponent n_r.

Index	Epoch (YYYY/MM)
1	2003/07
2	2004/10
3	2005/12
4	2006/09
5	2007/02
6	2008/08
7	2009/07
8	2010/01
9	2011/04
10	2012/09
11	2013/04
12	2014/06
13	2015/02
14	2016/11

3.3.4 Ensemble estimation and uncertainty

For each combination of two simulation case IDs i and j (corresponding to the cases listed in Table 2), selected gravity field epoch t and tuning constant c, an individual estimate of the orbital radius exponent $n_r^{(i,j,t,c)}$ is obtained from the regression described above. The final parameter value is defined as the median of the resulting ensemble:

$$n_r = \text{median}\left(n_r^{(i,j,t,c)}\right), \tag{15}$$

where (i, j, t, c) denotes the simulation pair, gravity field epoch, and Tukey bisquare tuning constant c.

The associated uncertainty is quantified using median absolute deviation (MAD). Assuming an approximately Gaussian distribution, the MAD is converted to an equivalent *robust standard deviation* using:

$$\sigma_{n_r} = 1.4826\,\text{median}\left(|n_r^{(i,j,t,c)} - \text{median}(n_r^{(i,j,t,c)})|\right). \tag{16}$$

The derived correction is validated in three independent steps. First, the scaling behaviour is independently assessed from a theoretical perspective using approximate degree variance spectra (App. C). This analysis provides an analytical estimate of the altitude dependence and supports the adopted power-law formulation, thereby offering an additional consistency check on the empirically derived exponent n_r. Secondly, it is applied within the simulation environment to assess residual errors in the KBR observables under the aforementioned controlled orbital configurations (App. D). And lastly, the correction factor is evaluated using real GRACE data by propagating the correction through the full processing chain and analysing its impact on monthly EWH estimates (see Eq. 17) derived from $\hat{K}$ (see Sect. 5.1.3).

3.4 Transforming ranging observables to EWH

After correcting for orbital geometry effects, the resulting KBR-derived observables represent spatially and temporally consistent proxies of mass variability. However, their amplitudes remain expressed in the observation domain and therefore require an empirical transformation into geophysical units. In this study, the corrected observable $\hat{K}$ (derived from either residual LGDs or residual ranges; see Sect. 3.1-3.2) is related to EWH anomalies h [cm] through a spatially resolved linear regression:

$$h = S\,\hat{K} + B + \epsilon, \tag{17}$$

where S and B denote the regression parameters, hereafter referred to as the *scale parameter*, and *bias* terms, respectively. The term ϵ represents the error related to regression, and L2-associated uncertainties. The regression is carried out in the time domain independently for each grid cell using the synthesised monthly Level-2 solutions h_{L2} (Sect. 2.3) and the corresponding monthly gridded geo-fit observables $\hat{K}$. This approach extends the framework of Spero (2021) and Zhu et al. (2025) by introducing a spatially distributed formulation, in which S and B are defined as spatially varying grids rather than aggregate (domain-averaged) quantities.

To obtain sub-monthly (5-day) mass change estimates, we assume that the scale parameter S, derived from the monthly observable-to-EWH relationship (Eq. 17), is equally applicable to the sub-monthly variations of the ranging observable, i.e. $\delta\hat{K}^{\mathrm{5d}}$. This assumption is partially assessed through the analysis of consecutive 5-day differences presented in Sect. 5.5. Under this assumption, the fitted parameters S and B are applied to the high-frequency geo-fit grids $\hat{K}^{\mathrm{5d}}$ (Eq. 9), yielding

$$h^{\mathrm{5d}} = S\,\hat{K}^{\mathrm{5d}} + B. \tag{18}$$

3.5 Hybridisation of ranging observables

Although the empirical observable-to-EWH transformation described in Sect. 3.4 can be applied independently to residual LGD and residual-range observables, LGD-based solutions may exhibit localised regression errors in regions of strong mass variability. Initial experiments using only residual LGDs revealed such artefacts over the Amazon basin, southern Greenland, and coastal Antarctica (see Sect. 5.2). These patterns are related to the spatial response of the LGD observable, where side-lobe structures can redistribute strong signals into neighbouring regions and introduce apparent mass variations.

Residual ranges provide a complementary response, exhibiting reduced side-lobe effects but weaker spatial localisation of the underlying mass anomalies (see Fig. 2). To combine the advantages of both observables, a hybrid gridded ranging-based residual observable is defined as

$$\hat{K}_{\mathrm{obs}} = \alpha\,(\delta g_{||})^{\mathrm{tn}} + (1-\alpha)\,(-\delta\rho)^{\mathrm{tn}}, \tag{19}$$

where $\alpha \in [0, 1]$ is the weighting factor between the residual LGD and range components. The superscript "tn" indicates temporal normalisation of a time series of grids $u(t, \lambda, \phi)$, where each grid cell is normalised by its time series standard deviation:

$$(u)^{\mathrm{tn}} = \frac{u}{s_u}, \quad s_u(\lambda, \phi) = \mathrm{std}\left\{u(t, \lambda, \phi)\right\}, \tag{20}$$

where s_u represents the temporal standard deviation computed independently for each grid cell, resulting in a spatially varying standard deviation grid. The negative sign applied to the range term accounts for the opposite phase response between range and LGD: a positive mass anomaly with respect to the mean induces a negative LGD peak and a positive range perturbation (Ghobadi-Far et al. 2018).

A one-dimensional synthetic example is used to illustrate how the hybrid observable K_{obs} balances the different spatial responses of the residual LGD and range components (Fig. 2). The along-track mass anomaly sequence is arbitrarily defined in terms of anomaly magnitude and position to demonstrate the effect of varying α between 0 and 1. The LGD component provides a sharper spatial response, allowing closely spaced anomalies to be distinguished (e.g., anomalies #2 and #6 from left to right), but exhibits pronounced side-lobe structures around large signals. In contrast, the residual range component reduces these oscillatory responses at the expense of a smoother spatial representation. Intermediate values of α therefore provide a compromise between spatial localisation and side-lobe mitigation. In practice, $\alpha_{\mathrm{opt}}(\lambda, \phi)$ is determined empirically through a discrete grid search, evaluating α values between 0 and 1 in increments of 0.1 and selecting the value that minimises the regression error (see Sect. 4.6) when relating K_{obs} to mass anomalies (Sect. 3.4).

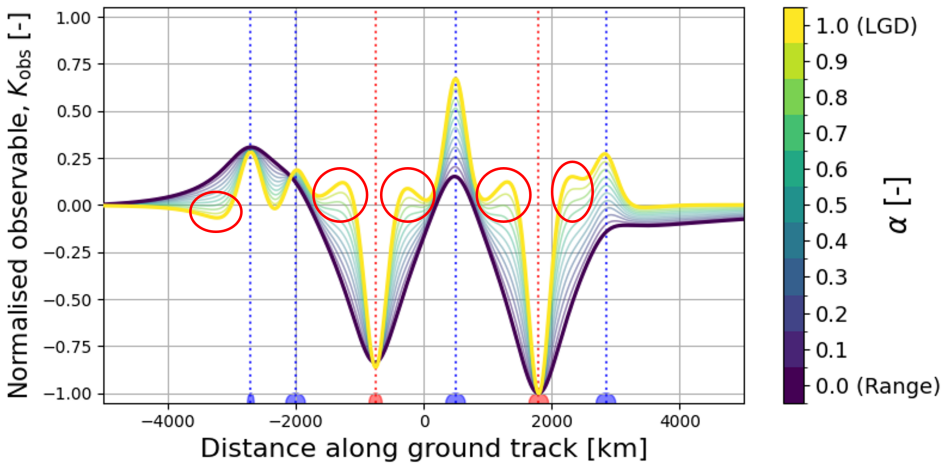


Fig. 2 Visualisation of the normalised hybrid observable K_{obs} as a function of along-orbit distance (in km) for different weighting factors α, ranging from 0 (pure residual range) to 1 (pure residual LGD). The side lobes highlighted in red illustrate the high-frequency content characteristic of LGDs. A schematic representation of the mass anomalies is shown at the bottom, where red half-ellipses denote positive density perturbations and blue ones denote negative ones. The six simulated disk anomalies have density anomalies –1500, –100, +1000, –300, +500, and –100 kg/m^2 and radii 50, 150, 100, 150, 150, and 150 km.

4 Uncertainty Estimation

To enable quantitative interpretation of the 5-day EWH solutions and their potential use in data assimilation applications, the uncertainty is propagated throughout the proposed processing chain (Sect. 3). The uncertainty budget comprises three categories: (i) observation-related uncertainties associated with the KBR-derived proxies (measurement noise, spatial interpolation, and transfer-function errors), (ii) uncertainties introduced by the empirical observable-to-EWH transformation, and (iii) uncertainties inherited from the monthly EWH grids derived from standard Level-2 solutions. The individual uncertainty components, their estimation procedures, and their spatial and temporal representation within the uncertainty propagation are summarised in Table 4. These contributions are subsequently propagated and combined into the final EWH uncertainty estimate (Sect. 4.8).

Table 4 Summary of uncertainty components considered in the sub-monthly TUD EWH gridded solutions. All spatial fields are provided on a $0.5° \times 0.5°$ latitude–longitude grid. The representation indicates whether the uncertainty is treated as a scalar value, a time-independent grid, or a time-varying grid.

Category	Representation	Time resolution	Section
Ranging observation			
Instrument noise	Scalar value	N.A.	Sect. 4.1
Altitude- and range-correction	Time-varying grid	5-day	Sect. 4.2
Spatial interpolation	Time-varying grid	5-day	Sect. 4.3
Transfer function	Time-independent grid	N.A.	Sect. 4.4
Hybridisation of ranging observables	–	–	Sect. 4.5
Observable-to-EWH conversion			
Regression uncertainty	Time-varying grid	5-day	Sect. 4.6
Monthly Level-2 solutions			
Level-2 ensemble uncertainty	Time-varying grid	Monthly	Sect. 4.7
AOD1B uncertainty	Time-varying grid	Monthly	Sect. 4.7

It is important to note that some uncertainty components, specifically the interpolation and transfer-function uncertainties, are estimated through dedicated numerical simulations performed with the open-source *Tudatpy* software (Dirkx et al. 2022). These simulations follow the same propagation setup described in Sect. 3.3.3, using an initial altitude of 450 km and an inter-satellite range of 220 km, and are performed for all CSR RL06 GRACE monthly solutions spanning April 2002 to June 2017.

4.1 Instrument uncertainties

The instrumental noise contribution is quantified separately for the two KBR-derived observables: residual LGD and residual range. The corresponding uncertainty components ($\sigma_{\delta g_{||},\mathrm{inst}}$ and $\sigma_{\delta\rho,\mathrm{inst}}$) represent the measurement noise propagated through the same processing steps applied to the observations, including the band-pass filtering applied to isolate the high-frequency signals. For clarity, we first consider the residual range noise component, expressed as

$$\sigma^2_{\delta\rho,\mathrm{inst}} = \int_{f_{\min}}^{f_{\max}} A^2_{\mathrm{inst}}(f)\, df, \tag{21}$$

where $f_{\min}$ and $f_{\max}$ denote the lower and upper limits of the band-pass filter applied to the residual range-rate time series (0.9–11 mHz). The total amplitude spectral density (ASD), denoted as $A(f)$, of the instrument noise is the sum of the K-band ranging (KBR) and accelerometer (ACC) contributions,

$$A^2_{\mathrm{inst}}(f) = A^2_{\mathrm{KBR}}(f) + A^2_{\mathrm{ACC}}(f), \tag{22}$$

where each term follows the analytical noise models of Müller (2017), assuming an inter-satellite separation of $L = 220$ km.

The LGD noise level is derived analogously from the range-acceleration, by applying the 2^{nd}-order differentiator $(2\pi f)^2$ to the range noise in the frequency domain and the transfer function $Z(f)$:

$$A_{\delta g_{||},\mathrm{inst}}(f) = Z(f)\, A_{\delta\ddot{\rho},\mathrm{inst}}(f) = Z(f)\, (2\pi f)^2\, A_{\mathrm{inst}}(f). \tag{23}$$

Fig. 3 illustrates the analytical amplitude spectra for both observables. The accelerometer noise dominates the residual range (see orange curve in Fig. 3a), while KBR noise becomes more significant for the range acceleration in the high-frequency domain (see blue curve in Fig. 3b) due to the amplification of high-frequency noise (above approx. 10 mHz) by the differentiation operator.

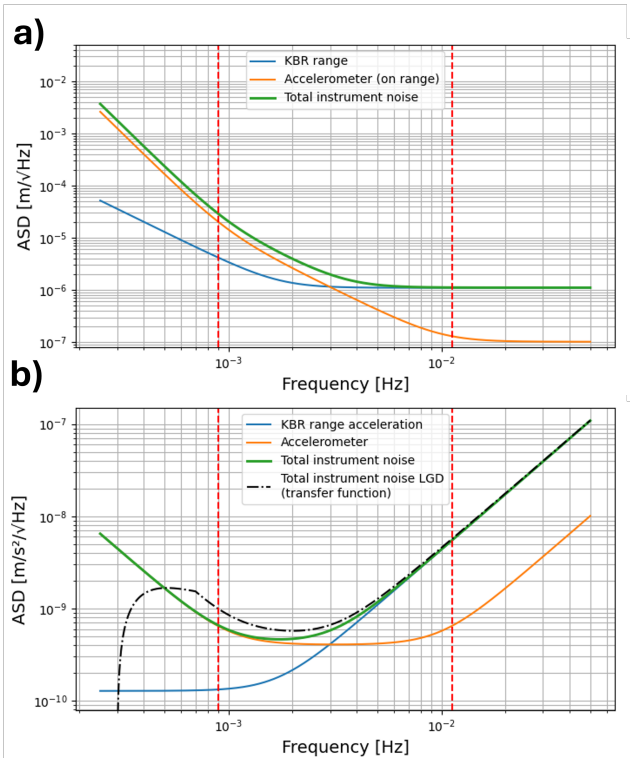


Fig. 3 Analytical amplitude spectral densities of the KBR and accelerometer noise for the **(a)** range and **(b)** range acceleration observables, respectively (Müller 2017). The resulting noise spectrum for the Line-of-Sight Gravity Difference (LGD) using the transfer function (Ghobadi-Far et al. 2018), is represented with a dot-dashed curve in **(b)**. The shaded vertical lines indicate the frequency band (0.9–11 mHz).

Integrating over the frequency band yields the noise level characteristics summarised in Table 5. A slight increase (from 0.26 to 0.28 nm/s^2) in noise is observed when converting from range acceleration to LGD (Fig. 3b), which is caused by the transfer function $Z(f)$ applied in this conversion. The magnitude of $Z(f)$ reaches approximately 1.5 at $f = 0.9$ mHz (Ghobadi-Far et al. 2018), resulting in a modest amplification of low-frequency accelerometer noise.

Table 5 Summary of integrated instrumental noise levels over the operational band (0.9–11 mHz) using analytical spectral density models (Müller 2017).

Observable	Symbol	Noise level
Residual range	$\sigma_{\delta\rho,\mathrm{inst}}$	0.42 μm
Residual range acceleration	$\sigma_{\delta\ddot{\rho},\mathrm{inst}}$	0.26 nm/s^2
Line-of-Sight Gravity Difference	$\sigma_{\delta g_{\|\|},\mathrm{inst}}$	0.28 nm/s^2

4.2 Uncertainty of the altitude- and range-correction factor

The uncertainty of the correction factor is derived by propagating the uncertainty of the estimated orbital radius exponent n_r (Sect. 3.3). From Eq. 12, the time dependent empirical correction factor is defined as

$$C(t) = \left(\frac{\bar{r}(t)}{\bar{r}_{\text{ref}}}\right)^{n_r} \left(\frac{\rho(t)}{\rho_{\text{ref}}}\right)^{n_L}, \tag{24}$$

where n_L is set to -1 (see Sect. 3.3). Assuming the uncertainty of n_L is negligible compared to that of n_r ($\sigma_{n_L} \ll \sigma_{n_r}$, see Sect. 3.3), the variance of the correction factor, σ_C^2, can be approximated using standard error propagation as

$$\sigma_C \approx C \left|\ln\left(\frac{\bar{r}}{\bar{r}_{\text{ref}}}\right)\right| \sigma_{n_r}. \tag{25}$$

In order to quantify the uncertainty in the corrected and gridded observable $K_{\text{obs}}^{\text{ref}}$, the uncertainty in the empirical correction factor $C(t)$ is propagated accordingly given the gridding operations discussed in Sect. 3.2, resulting in:

$$\sigma^2_{\hat{K}_{\text{ref}}} \approx \mathcal{G}\{\sigma_C^2(t)K^2(t) + C^2(t)\sigma_K^2\}, \tag{26}$$

where σ_K^2 corresponds to the instrument noise variance described in the previous section, and $\mathcal{G}\{\cdot\}$ denotes the gridding operators applied to the geo-fit and post-fit residuals time series (see Sect. 3.2). The uncertainties introduced by the gridding operations themselves are discussed in the following section.

4.3 Spatial interpolation uncertainties

Interpolation uncertainties arise when gridding or mapping gravity observables onto a common spatial grid (see Sect. 3.2). The two contributions are: mesh refinement of monthly geo-fits (Sect. 4.3.1), and 5-day spatial interpolation error (Sect. 4.3.2). We limit our analysis in this section to LGDs interpolation errors; however, the same procedure has been implemented for the residual range observable. For clarity, the observable symbol (K_{obs}, $\delta g_{||}$ or $\delta\rho$) is therefore omitted from the interpolation error notation.

4.3.1 Regridding of monthly geo-fit LGDs and ranges

To quantify the error introduced by spatial refinement ($\sigma_{\text{ref,int}}$), the monthly geo-fit solutions were first aggregated onto a coarse $2^\circ \times 2^\circ$ grid and subsequently interpolated to the finer $0.5^\circ \times 0.5^\circ$ analysis mesh (resulting in $\hat{K}(\lambda, \phi)$). The corresponding interpolation (or refinement) errors were evaluated through forward simulations using the monthly spherical harmonic solutions (see the *Tudatpy* simulation setup in Sect. 3.3). Figure 4 illustrates both the temporal evolution of the global RMS error (Fig. 4a) and representative spatial patterns for selected epochs, highlighting variability linked to data coverage (Fig. 4a,b) and orbit geometry (Fig. 4d).

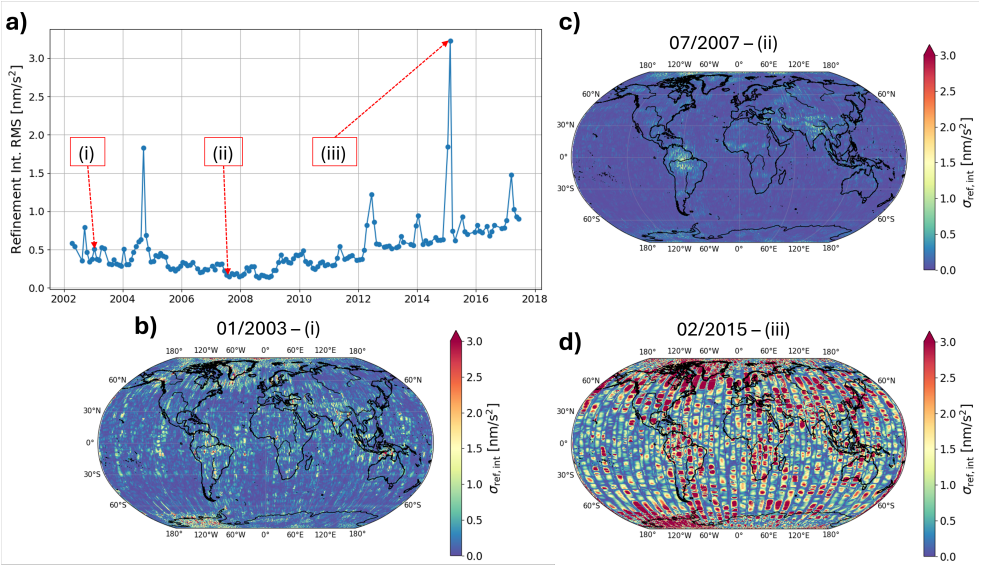


Fig. 4 Temporal and spatial characteristics of the interpolation (refinement) error in the case of Line-of-Sight Gravity Difference observable. **(a)** Global RMS as a function of time, with annotations (i)–(iii) marking selected epochs. **(b)**–**(d)** Spatial patterns for (i) January 2003 (reduced coverage), (ii) July 2007 (nominal conditions), and (iii) February 2025 (most significant repeat orbit pattern).

During nominal mission periods (2005–2011), the interpolation (refinement) error remains small, with global RMS values well below 0.5 nm/s^2 (Fig. 4a, annotation (ii)). Spatially, errors are largely confined to narrow, stripe-like features over regions of strong gravity signal (Fig. 4c), including the Amazon, Ganges–Brahmaputra, central African river basins, West Antarctica, and southern Greenland, where local values reach up to 1.5 nm/s^2. In contrast, during non-nominal periods characterised by reduced sampling, such as January 2003 (approximately 40% fewer L1B 5-s observations), the interpolation error increases globally to 0.5–0.75 nm/s^2 (Fig. 4a, annotation (i)), reflecting the degraded ground-track coverage. The corresponding spatial patterns (Fig. 4b) show enhanced but still localised errors up to 2–2.5 nm/s^2 over the same high-signal regions. Finally, during repeat orbit resonances, when the satellite ground tracks recur with near-identical geometry, the interpolation error increases substantially (Fig. 4a, annotation (iii)), with global RMS values of 1.5–3.25 nm/s^2 and spatial patterns exceeding 5-15 nm/s^2 in error magnitude (Fig. 4d).

4.3.2 Post-fit residuals interpolation errors

The 5-day subsets of post-fit residual LGD and range data are spatially interpolated directly onto the common $0.5° \times 0.5°$ analysis grid. Unlike the monthly geo-fit products, the "true" interpolation error of these residuals cannot be directly simulated, as they are inherently linked to CSR's Level-2 gravity field retrieval from Level-1B data. To approximate this error, an empirical scaling approach is employed:

$$\sigma_{5\mathrm{d,int}} \approx S_R \, \sigma_{5\mathrm{d,int}}^{(\text{sim. geo-fit})}, \tag{27}$$

where $\sigma_{5\mathrm{d,int}}^{(\text{sim. geo-fit})}$ is estimated using the absolute spatial interpolation error derived from the forward simulation of 5-day geo-fit LGD and range, and the scaling factor S_R is determined as

$$S_R = \frac{\mathrm{RMedS}_{\text{post-fit res.}}}{\mathrm{RMedS}_{\text{geo-fit}}}, \tag{28}$$

with RMedS denoting the *Root Median Square*, a robust alternative to the RMS that is less sensitive to outliers (we refer the reader to App. B for more details).

In Fig. 5, an overview of the temporal (Fig. 5a,b) and spatial (Fig. 5c,e) behaviour of these empirically scaled 5-day interpolation uncertainties, highlighting their variability across representative mission periods and orbital configurations.

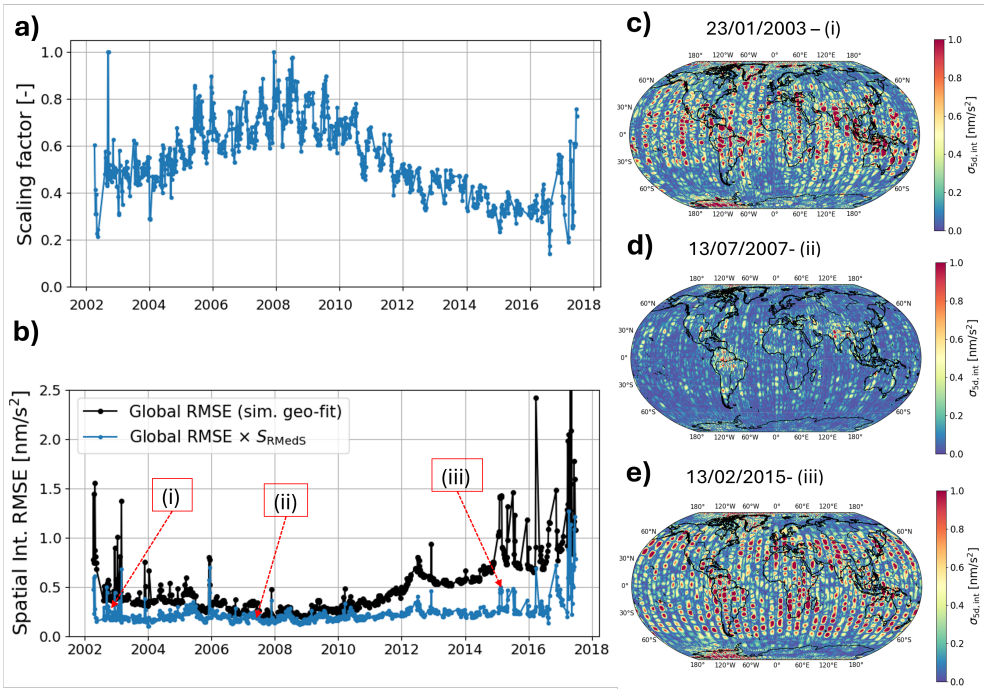


Fig. 5 Temporal and spatial characteristics of the direct spatial interpolation error in the case of 5-day sets of Line-of-Sight Gravity Differences. **(a)** Scaling factor S_R derived from the RMedS estimator, **(b)** global RMS of the 5-day spatial interpolation error time series with annotated periods: (i) 23 Jan 2003 (reduced sampling), (ii) 13 Jul 2007 (nominal conditions), and (iii) 13 Feb 2015 (most significant orbit repeat pattern), corresponding to subplots **(c)**–**(e)** showing their respective spatial error distributions.

Similar to the mesh refinement errors discussed in the previous section, the 5-day interpolation uncertainties exhibit pronounced spatial patterns near geophysically

active regions. These patterns reflect the direct spatial interpolation of scattered orbital data and are particularly sensitive to outliers and irregular sampling in the residual time series. Globally, RMS values reach 0.5–0.75 nm/s^2 (Fig. 5b). Spatially, uncertainties are typically 0.5–0.6 nm/s^2 during nominal periods (Fig. 5d), but can increase to 0.5–3 nm/s^2 during non-nominal periods (Fig. 5c,e). Overall, the 5-day interpolation uncertainties range from approximately 30% to 80% of the magnitude of the mesh refinement error, indicating a secondary but non-negligible contribution to the total interpolation uncertainty. As expected, the interpolation uncertainty decreases with longer accumulation periods, owing to the increased spatial coverage available to the interpolation procedure (not shown).

4.4 Transfer function uncertainty

The transfer function uncertainty is quantified exclusively for the LGD observable, as the transfer function is only applied to transform range accelerations into LGDs. It is computed as the temporal RMS of the resulting gridded transfer-function residuals at each grid cell:

$$\sigma_{\mathrm{TF}}(\lambda,\phi) = \sqrt{\frac{1}{N_t}\sum_{i=1}^{N_t}\left(\hat{\Delta}_{\mathrm{TF}}(t_i,\lambda,\phi)\right)^2}, \tag{29}$$

where $\hat{\Delta}_{\mathrm{TF}}(t_i,\lambda,\phi)$ denotes the gridded transfer-function errors at monthly epoch t_i, N_t denotes the number of CSR RL06 monthly solutions considered, and t_i represents the individual monthly gravity-field solutions spanning the GRACE mission period. The residuals are obtained as the difference between the simulated monthly LGDs and the LGD estimates obtained by applying the transfer function derived by Ghobadi-Far et al. (2018) to the simulated range acceleration observations as described in Eq. 4. The resulting transfer-function residuals are subsequently converted into latitude–longitude grids following the procedure described in Sect. 3.2.1, yielding the gridded temporal sequence $\hat{\Delta}_{\mathrm{TF}}(t_i,\lambda,\phi)$ used for the RMS calculation. The resulting σ_{TF} is consequently an uncertainty grid. Figure 6 shows the spatial distribution of the resulting uncertainty.

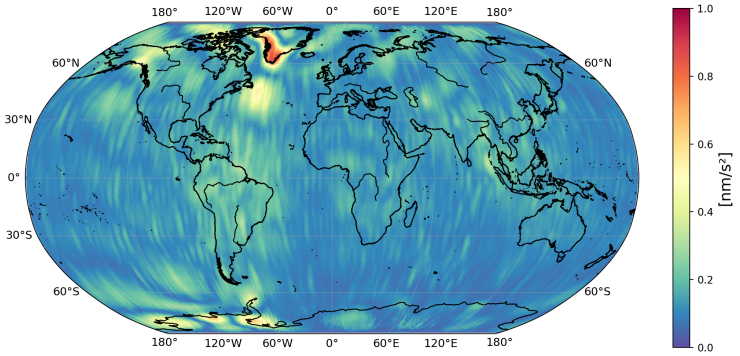


Fig. 6 Spatial distribution of the simulated transfer function uncertainty component (σ_{TF}), derived from the analytical fit of the spectral admittance described in Ghobadi-Far et al. (2018) and approximated by the temporal root-mean-square (RMS) of the monthly grids of simulated Δ_{TF} values.

As shown in Fig. 6, the transfer function error over land generally ranges from 0.25-0.4 nm/s^2, while over the oceans it is slightly lower, typically 0.15–0.4 nm/s^2. The largest errors occur along the Greenland coast (0.8 nm/s^2) and along the western Antarctic coast (0.5–0.7 nm/s^2). Compared to the interpolation errors, this component is significant during nominal mission periods and should be retained. However, during orbit repeat pattern phases, its contribution becomes negligible relative to the 5-day and monthly refinement errors (see Fig. 4d and 5e).

4.5 Uncertainty of the hybrid ranging observable

The uncertainty of the hybrid observable $\hat{K}_{\mathrm{obs}}$ is obtained by propagating the uncertainties of the two corrected KBR-derived components (Sect. 3.5). Considering the correlation between the residual LGD and range observables, the variance is expressed as

$$\sigma^2_{\hat{K}_{\mathrm{obs}}} = \alpha^2 \frac{\sigma^2_{\delta g_{||}}}{s^2_{\delta g_{||}}} + (1-\alpha)^2 \frac{\sigma^2_{\delta\rho}}{s^2_{\delta\rho}} - 2\alpha(1-\alpha) r_c \frac{\sigma_{\delta g_{||}}}{s_{\delta g_{||}}} \frac{\sigma_{\delta\rho}}{s_{\delta\rho}}, \tag{30}$$

where r_c is the Pearson correlation coefficient between $\delta g_{||}$ and $\delta\rho$.

The residual LGD uncertainty is composed of instrumental noise, spatial interpolation uncertainty, and the uncertainty associated with the transfer-function correction:

$$\sigma^2_{\delta g_{||}} = \sigma^2_{\delta g_{||},\mathrm{inst}} + \sigma^2_{\delta g_{||},\mathrm{int}} + \sigma^2_{\mathrm{TF}}. \tag{31}$$

Similarly, the residual range uncertainty is given by

$$\sigma^2_{\delta\rho} = \sigma^2_{\delta\rho,\mathrm{inst}} + \sigma^2_{\delta\rho,\mathrm{int}}. \tag{32}$$

The individual contributions are quantified in Sects. 4.1–4.4.

4.6 Regression uncertainty

The uncertainty associated with the regression coefficients $\hat{\mathbf{x}} = [S, B]^\top$, with scale parameter S and bias B (see Sect. 3.4), is computed using

$$\sigma^2_{h,\mathrm{reg}} = \mathbf{p}^\top \Sigma_{\hat{\mathbf{x}}} \mathbf{p}, \tag{33}$$

where $\Sigma_{\hat{\mathbf{x}}}$ is their covariance matrix, and $\mathbf{p}$ is the vector

$$\mathbf{p} = \frac{\partial h}{\partial \widehat{\mathbf{x}}} \tag{34}$$

containing the partial derivatives of EWH with respect to the regression parameters.

The covariance matrix is estimated under the assumption of white, uncorrelated noise

$$\Sigma_{\hat{\mathbf{x}}} \approx \hat{s}^2 (\mathbf{R}^\top \mathbf{R})^{-1}, \tag{35}$$

where $\mathbf{R}$ is the design matrix corresponding to the linear relation in Eq. 17, and $\hat{s}$ is the unbiased standard deviation of the residuals between the estimated EWH and the reference EWH derived from the CSR RL06 Level-2 solutions (see Sect. 2.3). This regression-derived uncertainty is minimised when determining the optimal weighting parameter α (see Sect. 3.5), ensuring the most consistent agreement between the empirically retrieved and reference EWH grids.

4.7 Gridded EWH uncertainties from Level-2 solutions

The final uncertainty component represents the uncertainty associated with the monthly EWH solutions derived from the Level-2 gravity field estimates. Several approaches have been proposed to quantify Level-2 uncertainties, including full variance–covariance propagation and empirical approximations based on spatial and temporal variability (e.g., Boergens et al. 2022). We follow the empirical ensemble-based uncertainty estimation methodology described in Cuadrat-Grzybowski et al. (2026a), while applying the same filtering strategy as used for the EWH solutions, including DDK3 filtering and the corresponding low-degree truncation (see Sect. 2.3).

The monthly EWH uncertainty is estimated as the weighted unbiased ensemble standard deviation of the Level-2 solutions, with an additional contribution from AOD1B model uncertainty:

$$\sigma^2_{h,\mathrm{L2}} = \frac{1}{1 - \sum_{i=1}^{N} \bar{w}_i^2} \sum_{i=1}^{N} \bar{w}_i \left(h_i - \overline{h}\right)^2 + \sigma^2_{h,\mathrm{AOD1B}}, \tag{36}$$

where h_i denotes the monthly EWH solution from the i^{th} processing centre after filtering (Sect. 2.3), $\overline{h}$ is the weighted ensemble mean, and N is the number of solutions considered (see Sect. 2.2.1). The normalised weights $\bar{w}_i$ are computed from the inverse squared monthly ocean residual RMS with respect to COST-G RL02.1. The additional term $\sigma_{h,\mathrm{AOD1B}}$ accounts for uncertainty associated with the non-tidal atmosphere and ocean de-aliasing model. Further details on the uncertainty estimation methodology are provided in Cuadrat-Grzybowski et al. (2026a).

4.8 Combining all uncertainties

The total uncertainty of the estimated EWH is obtained by combining the independent uncertainty contributions described above:

$$\sigma_h^2 = \left(\frac{\partial h}{\partial \hat{K}}\right)^2 \sigma_{\hat{K}}^2 + \sigma_{h,\mathrm{reg}}^2 + \sigma_{h,\mathrm{L2}}^2, \tag{37}$$

where $\hat{K}$ denotes the gridded ranging observable, either the LGD or residual-range formulation (Sect. 3.1), or the hybrid observable $\hat{K}_{\mathrm{obs}}$ (Sect. 3.5), and $\sigma_{\hat{K}}^2$ denotes its variance (Sect. 4.5). The first term in Eq. 37 represents the contribution from the observation uncertainty (measurement noise and interpolation error), the second term accounts for the uncertainty in the regression model represented in Eq. 17 as described in Sect. 4.6, and lastly, the third term relates to the uncertainties related to the monthly EWH grids obtained from Level-2 solutions (Sect. 4.7). These components are assumed to be independent of each other.

5 Results and Discussion

This section presents the evaluation and characterisation of the proposed high-frequency EWH solutions. First, the altitude- and range-dependent correction is assessed in Sect. 5.1, including the estimation of the orbital radius exponent, the propagation of its uncertainty into the correction factor, and its validation using the GRACE swap manoeuvre experiment. Next in Sect. 5.2, the spatial characteristics of the observable-to-EWH transformation are analysed. The performance of the derived 5-day solutions is then evaluated against state-of-the-art ITSG-Grace2018 daily solutions in Sect. 5.3, first through a global spatio-temporal comparison and subsequently through dedicated geophysical case studies. The uncertainty budget is then quantified for all three formulations (LGD-, range-, and hybrid-based solutions), including the additional uncertainty introduced relative to monthly EWH products (Sect. 5.4). Finally, the temporal consistency and limitations of the 5-day solutions are investigated through an analysis of consecutive 5-day differences across month boundaries (Sect. 5.5).

5.1 Empirical correction of observables for orbital variations

5.1.1 Orbital radius exponent

Following the methodology outlined in Sect. 3.3, the orbital radius exponent n_r is inferred from the ensemble of synthetic simulation case studies. The resulting estimates and their associated uncertainties are summarised in Table 6, with a more detailed presentation of the simulation results provided in App. D.

The simulation-derived estimates are quantitatively consistent with the analytical expectations. For LGD, the analytical scaling predicts an orbital radius exponent of $n_r = 15.184$ with a relative uncertainty of approximately 3.3% (App. C), while the simulation-based estimate yields $n_r = 14.874$ with a relative uncertainty of about 5.1%. For the residual range observable, the analytical prediction of $n_r = 9.305$ with

Table 6 Estimated orbital radius exponent n_r and associated uncertainty σ_{n_r} for the two observables considered. These estimates are obtained by fixing the range exponent $n_L = -1$.

Observable	n_r [-]	σ_{n_r} [-]
Line-of-sight Gravity Difference	14.874	0.762
Residual range	9.317	0.318

a relative uncertainty below 2.3% compares to a simulated value of $n_r = 9.317$ and a relative uncertainty of approximately 3.4%. In both cases, the inferred magnitudes closely match the theoretical values. The larger relative uncertainties obtained from the simulations are expected, as the analytical estimates are derived from altitude variations only, while the simulation ensemble includes cases in which altitude and inter-satellite range are varied simultaneously. Despite this increased complexity, the residual range exponent remains more tightly constrained than the LGD exponent in relative terms, consistent with the analytical scaling behaviour.

5.1.2 Temporal behaviour of the correction factor

Having established global values for the orbital radius exponent, the subsequent analysis focuses on the temporal evolution of the correction factor, $C(t)$, itself (see Eq. 24). Figure 7 shows the time series of the correction factor and its associated uncertainty (Fig. 7b), driven by variations in satellite altitude and inter-satellite range over the mission lifetime (Fig. 7a).

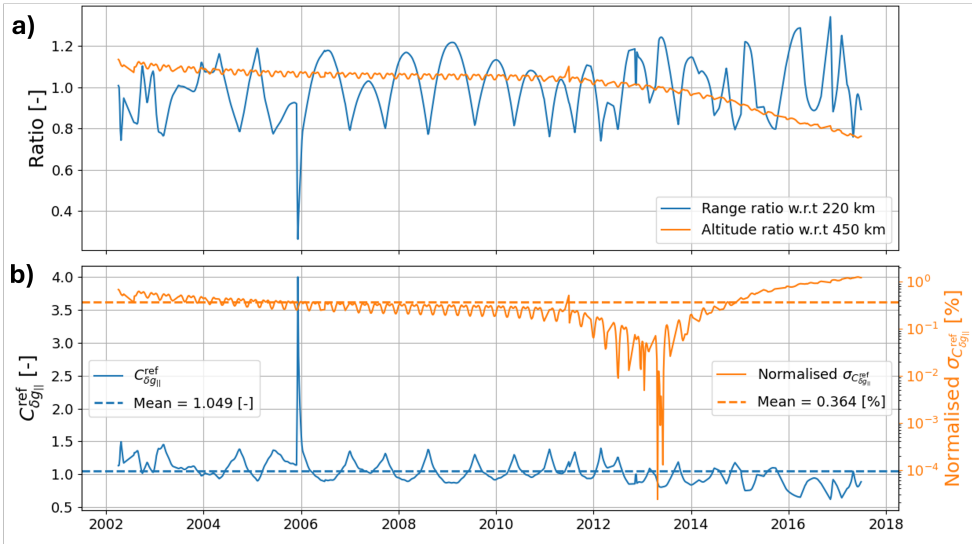


Fig. 7 Temporal evolution of the quantities entering the LGD correction factor. (a) Time series of 5-day median altitude (average of the twin satellites) and inter-satellite range ratios with respect to the reference values ($h_{\text{ref}} = 450$ km and $\rho_{\text{ref}} = 220$ km). (b) Corresponding 5-day median correction factor ($C^{\text{ref}}_{\delta g_{||}}$) for the LGD observable and its normalised uncertainty.

The altitude evolution is dominated by the long-term orbital decay, decreasing from approximately 530 km at the beginning of the mission to about 340 km towards the end (Fig. 7a), corresponding to a relative change from ∼1.1 to ∼0.75 with respect to the reference altitude of 450 km. Superimposed short-term oscillations in the mean altitude are negligible, with amplitudes below 0.03 in relative units and a characteristic period of approximately three months. In contrast, the inter-satellite range exhibits pronounced periodic variations with an approximate annual cycle and an amplitude of ∼0.2 in relative units (Fig. 7a). These two behaviours translate directly into the temporal variability of the correction factor (Fig. 7b), with the long-term trend controlled by altitude and shorter-term modulations driven by range variations.

The maximum correction factor, reaching values of up to ∼4, occurs during the period 6–10 December 2005, coinciding with the GRACE satellite swap (Fig. 7). This pronounced peak is not reflected in the uncertainty, as the contribution of the uncertainty in n_L has been neglected (Eq. 25) compared to that associated with the altitude-dependent term n_r. Conversely, a minimum in the uncertainty is observed between April and June 2013, when the mean altitude is closest to the reference altitude of 450 km.

Over the full mission, the mean correction factor is 1.049, indicating that LGD observations are, on average, only weakly affected. More precisely, the correction factor recurrently approaches unity approximately every 7–9 months, reflecting periods where the combined altitude and range conditions are close to their reference values. The normalised uncertainty remains small, with a mean value of 0.364% and a maximum of approximately 1% towards the end of the mission, when the altitude ratio deviates most from unity (Fig. 7b). However, the short-term variability of the correction factor, driven by inter-satellite range changes, reaches amplitudes of ∼0.4, corresponding to variations of up to 40% in LGD magnitude on annual timescales. This highlights the importance of accounting for the correction factor when analysing along-track LGD residuals.

5.1.3 Correction factor during GRACE satellite swap

The correction factors introduced to account for altitude and inter-satellite range dependency are evaluated using the GRACE satellite swap event in December 2005. During this period, the inter-satellite separation varied strongly from approximately 200 km to below 50 km (see Sect. 5.1.2, Fig. 7a), providing a clear experiment to test the stability of the corrected monthly LGD geo-fits under varying orbital configurations.

Figure 8 illustrates the impact of the correction for four different observational regimes within December 2005: (a) observations collected with inter-satellite range $\geq$ 175 km, (b) ranges between 100–135 km, (c) ranges below 90 km, and (d) the full gridded solution aggregated on a $2^\circ \times 2^\circ$ grid using the grid-cell median. Each panel is shown in two columns, where (i) corresponds to the uncorrected LGD geo-fits and (ii) to the corrected solutions. The actual mean orbital altitude during this month is approximately 480 km with a standard deviation of 14 km, while the inter-satellite range has a mean of about 114 km and a standard deviation of 33 km.

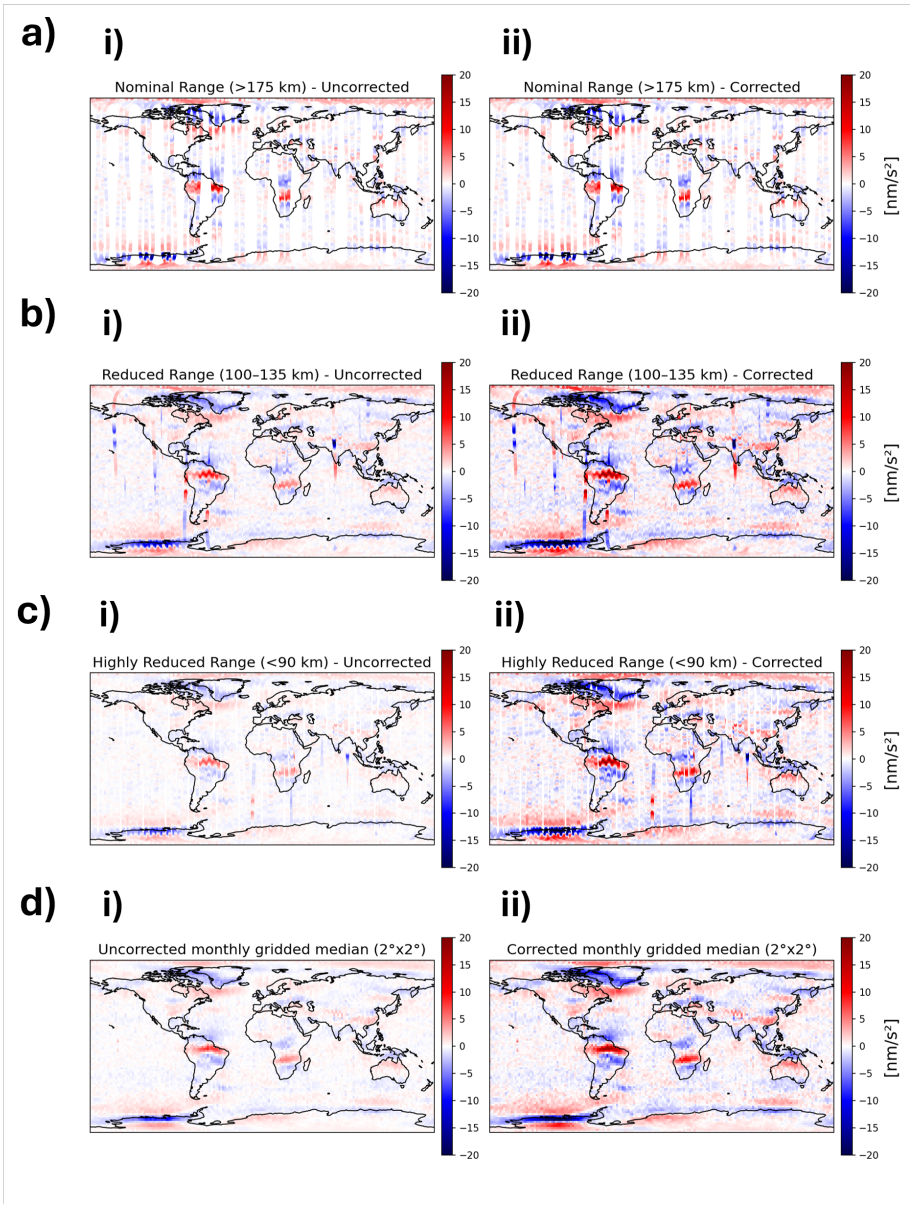


Fig. 8 LGD geo-fits during the December 2005 GRACE satellite swap, before (i) and after (ii) range and altitude normalisation. Panels (a)–(c) show progressively shorter inter-satellite ranges: $\geq$175 km, 100–135 km, and <90 km; panel (d) shows the monthly $2^\circ \times 2^\circ$ spatial-median grid. Corrections use $\rho_{\mathrm{ref}} = 220$ km and $h_{\mathrm{ref}} = 450$ km.

A clear and systematic dependency is observed in the uncorrected solutions (left column): as the inter-satellite range decreases, the magnitude of the LGD geo-fits is reduced. Since the geo-fits represent the same monthly gravity field expressed in

the observation domain, this geometry-dependent amplitude variation is undesirable. It would otherwise propagate into the empirical observable-to-EWH transformation (Eq. 17). This effect is particularly evident over the Amazon basin (see also Fig. 8a(i)–c(i)), where the signal amplitude decreases from approximately 15–17 nm/s^2 at large separation, to 7–10 nm/s^2 at intermediate ranges, and further below 5 nm/s^2 at the smallest separations. The corresponding monthly median reaches only about 5–6 nm/s^2 (Fig. 8d(i)).

When the correction factors are applied, the dependency is largely removed. The LGD geo-fits become substantially more stable over the full range of inter-satellite distances, with the Amazon basin signal recovering a consistent magnitude of approximately 17–20 nm/s^2 (Fig. 8a(ii)–c(ii)), and a monthly gridded median in the range of 15–20 nm/s^2 (Fig. 8d(ii)). Similar improvements are observed across other major hydrological and cryospheric regions, including the Central African river basins, northern Australia, the strong Antarctic coastal signals, and Greenland. These results provide strong conceptual support for the validity of the correction approach, demonstrating that it restores the expected monthly gravity field average.

We finally validate the use of the correction factor by comparing the monthly uncorrected and corrected geo-fits (no post-fits were considered for this test) after transformation into EWH against CSR RL06 monthly solutions. For brevity, only the hybrid observable is shown; however, similar improvements are obtained for both the LGD and range formulations, as these are linearly combined to form the hybrid observable. Figure 9 summarises this comparison: panel (a) shows the uncorrected monthly TUD hybrid EWH, with its corresponding error relative to CSR RL06 in (b). The corrected monthly TUD hybrid solution is shown in (c), with the associated error in (d). The CSR RL06 reference grid is provided in (e), while panel (f) presents the difference in absolute errors between (b) and (d), where negative (blue) values relate to an improvement due to the correction.

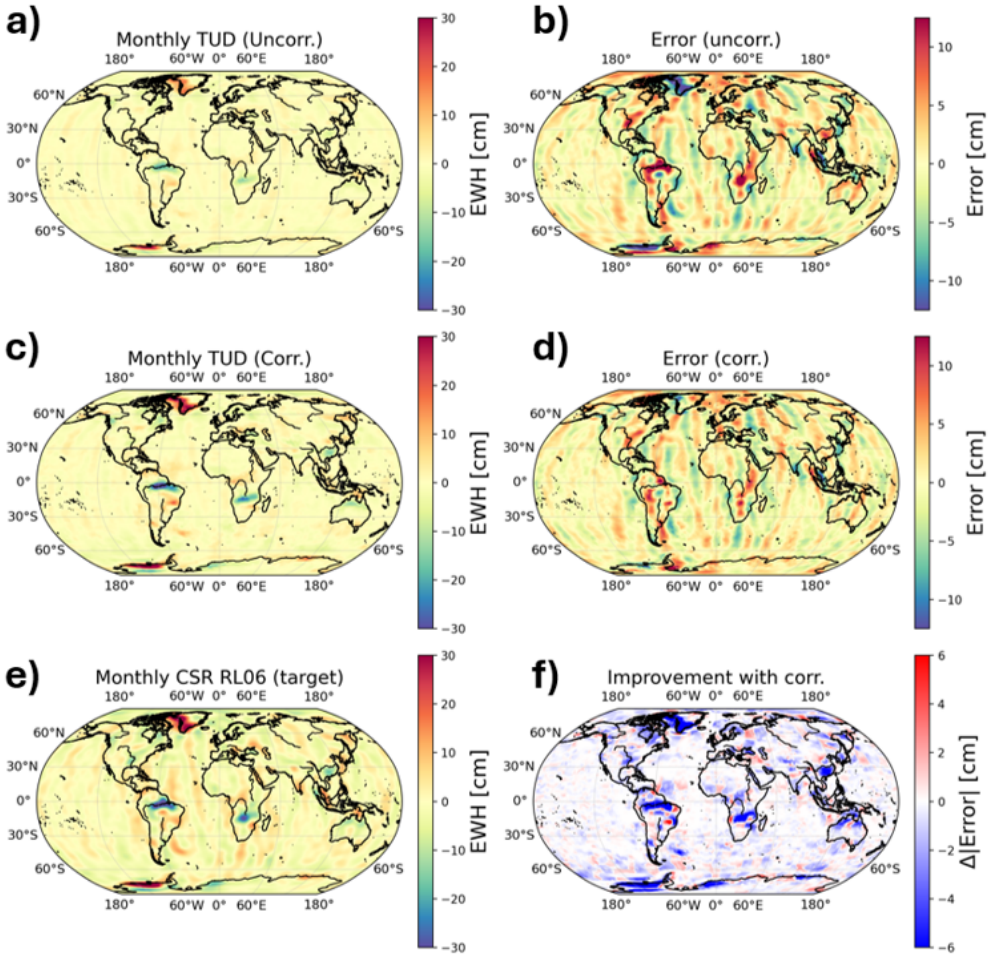


Fig. 9 Comparison of monthly TUD hybrid EWH solutions with CSR RL06 (December 2005). (a) Uncorrected TUD hybrid EWH. (b) Difference between uncorrected TUD hybrid and CSR RL06. (c) Corrected TUD hybrid EWH. (d) Difference between corrected TUD hybrid and CSR RL06. (e) CSR RL06 reference solution. (f) Difference in absolute errors between (b) and (d), where negative (blue) values indicate improvement after correction.

Without applying the correction (Fig. 9a), the reconstructed EWH amplitudes are systematically underestimated, leading to pronounced regional errors (Fig. 9b). These reach values of approximately +10 cm over the Amazon basin and up to −15 cm along the western coast of Greenland and north-western Antarctica. After applying the correction (Fig. 9c), the magnitude of the estimated EWH increases substantially, by up to a factor of four in regions of strong geophysical signal, resulting in a clear reduction of the corresponding errors (Fig. 9d). This improvement is confirmed in Fig. 9f, where reductions in absolute error of approximately 4–6 cm are observed in the aforementioned regions. Areas exhibiting negative improvement (shown in red

in Fig. 9) are primarily associated with north–south oriented noise patterns present in the CSR RL06 solutions (Fig. 9e), which are not observed in the monthly test solution using the proposed methodology. Overall, the results demonstrate that the correction significantly enhances the consistency of the reconstructed EWH grids with the reference solutions, particularly in regions of high signal amplitude.

5.2 Spatial characteristics of the ranging observable-to-EWH transformation

A key outcome of the proposed methodology is the derivation of spatially varying regression parameters that relate the ranging observables to equivalent water height. These parameters capture the regional variability in the observation-to-mass relationship and provide the basis for converting the corrected KBR-derived observables into EWH grids.

We first assess the performance of the empirical transformation (Eq. 17) using the LGD-only formulation. The resulting spatial distributions of the scale S (Fig. 10a) and bias B (Fig. 10b) parameters, together with the relative RMS of the regression error (Fig. 10c) and the Pearson correlation (Fig. 10d), are shown in Fig. 10.

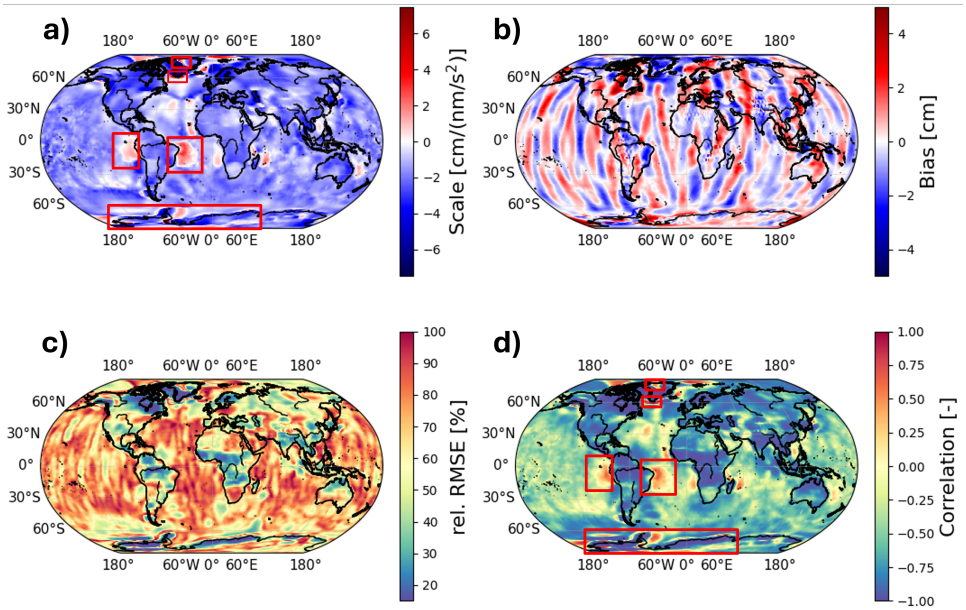


Fig. 10 Spatial distributions of the LGD-based empirical transformation parameters and performance metrics. (a) Scale S [cm/(nm/s^2)], (b) bias B [cm], (c) relative regression RMSE (ratio between RMS of regression error and RMS of the target EWH signal), and (d) Pearson correlation coefficient. Selected regions of strong geophysical variability are indicated in panels (a) and (d).

The spatial distribution of the scale parameter is predominantly negative (Fig. 10a), as expected from the physical relationship between LGD and mass anomalies. The global mean of the negative scale values is -1.74 cm/(nm/s^2). The bias term (Fig. 10b) exhibits alternating positive and negative north–south oriented stripes, reflecting the spatial imprint of residual noise in the Level-2 solutions, with a near-zero global mean of -0.03 cm. The correlation between the transformed observable and the target signal (Fig. 10d) is generally negative, with a global mean of -0.62 (considering regions with negative scale). In regions of strong geophysical variability, such as the Amazon basin, the Ganges–Brahmaputra basin, and central Africa, as well as regions affected by large seismic events (e.g. Sumatra 2004/12 and Tohoku 2011/03), the anti-correlation reaches values between -0.85 and -0.95 (Fig. 10d), indicating a strong consistency between the LGD-derived observable and the underlying mass signal. The relative regression RMSE (Fig. 10c) shows a consistent spatial pattern, with low values of approximately 5–20% in geophysically active regions, increasing to 30–50% over oceanic regions, and reaching up to 80-90% in quiet regions such as the Sahara, and even 90-100% in other noise-dominated regions.

Despite this overall agreement, pronounced artefacts are observed, particularly in regions adjacent to strong mass signals, such as to the east and west of the Amazon basin and across Greenland and Antarctica. In these polar regions, the artefacts extend from the coastal margins into the interior, particularly in southern Greenland and along the northern Antarctic sector (Fig. 10a,c,d). These artefacts manifest as localised areas of positive scale and correlation, which are physically inconsistent with the expected anti-correlation between LGD and mass anomalies. They are further associated with elevated relative RMSE values of 60–90% (Fig. 10c). These patterns are primarily attributed to inconsistencies between the spatial–spectral filtering applied to the LGD and residual-range observables and that inherent to the DDK3 smoothing and gentle truncation framework (App. A). This mismatch leads to a redistribution and smearing of spatially localised, high-amplitude signals, particularly in regions of strong geophysical variability such as the Amazon basin and the polar regions (Fig. 19a–d, subpanels iii), where the standard deviation of the temporal correlation grids highlights the increased sensitivity to the choice of filtering and truncation strategy. Lastly, in polar regions, this effect is further enhanced by north–south elongated side-lobe structures (Sect. 3.5), which amplify spatial leakage into surrounding oceanic areas.

To mitigate these effects, we re-introduce the normalised hybrid observable ($\hat{K}_{\mathrm{obs}}$) from Eq. 19. The corresponding spatial distributions of the scale (Fig. 11a), bias (Fig. 11b), relative regression RMSE (Fig. 11c), Pearson correlation (Fig. 11d), and optimal weighting factor α (Fig. 11e) demonstrate a reduction in these artefacts, especially visible in the interior of Greenland and Antarctica.

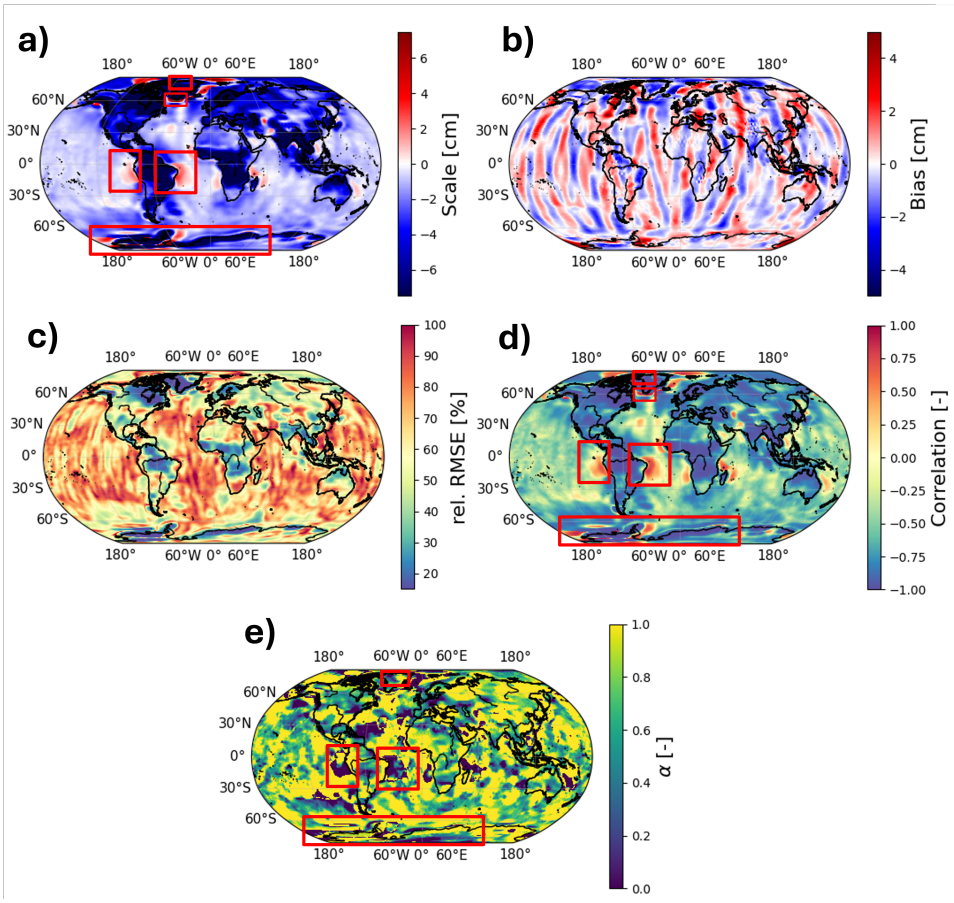


Fig. 11 Spatial distributions of the hybrid-observable-based empirical transformation parameters and performance metrics, using the normalised observable $\hat{K}_{\mathrm{obs}}$. (a) Scale S [cm], (b) bias B [cm], (c) relative regression RMSE (ratio between RMS of regression error and RMS of the target EWH signal), (d) Pearson correlation coefficient, and (e) optimal weighting factor α that minimises the regression error.

The scale parameter grid (Fig. 11a) shows a stronger spatial localisation of geophysical signals, compared to the LGD formulation (Fig. 10), particularly over land-dominated hydrological regions, major earthquakes (e.g. Sumatra 2004/12 and Tohoku 2011/03), and notably the Zapiola Rise in the Argentine Basin (east of Argentina). The scale remains predominantly negative, with a global mean (considering only negative values) of approximately -4 cm. In contrast, the hybrid-based bias term exhibits only minor changes relative to the LGD-only case, retaining similar spatial patterns (Fig. 11b) with a near-zero global mean of -0.036 cm. The correlation in regions with negative scale increases in magnitude to a global mean of -0.66 (Fig. 11d), with geophysically active regions (i.e. major river basins, the Zapiola rise and polar regions) showing a further improvement of approximately 0.025 in absolute terms.

The relative regression RMSE (Fig. 11c) is reduced overall compared to the LGD and range (not shown) formulations, with typical values decreasing to around 15–20% in strongly varying regions, approximately 25–50% over oceanic, and 80–90% in low-signal areas. Regions such as the interior of Greenland exhibit a substantial reduction in relative RMSE, from previously 60–90% to 15–50%, coinciding with a transition of the scale from positive to predominantly negative values. In contrast, regions adjacent to strong signals, such as the east–west regions next to the Amazon basin, still display positive scale values (Fig. 11a), although with a moderate reduction in relative RMSE of approximately 5–10%.

Importantly, the locations of improvement are closely linked to the spatial distribution of the weighting factor α (Fig. 11e). Regions with negative scale, where the physical relationship is correctly captured, correspond to high α values (mean ~ 0.75), indicating a dominant contribution from LGD. Conversely, regions with persistent positive scale (e.g., east-west lobes around the Amazon basin) exhibit lower α values (mean ~ 0.28), reflecting a stronger contribution from the residual range observable. This behaviour confirms that the hybrid formulation adaptively balances both observables to minimise the regression error and reduce side-lobe artefacts.

5.3 Validation of high-frequency (5-day) EWH solutions

The observable-to-EWH transformation derived in Sect. 3.4 is applied to the corrected KBR-based observables (discussed in Sect. 3.1) to obtain global 5-day EWH grids. These solutions provide a representation of sub-monthly mass variability beyond the temporal resolution of conventional monthly gravity-field products. Their performance is evaluated in Sect. 5.3.1 through comparison with the Kalman-filtered ITSG-Grace2018 daily solutions, assessing consistency in both the spatial and temporal domains. In addition, the ability of the product to capture high-frequency mass variations is demonstrated through selected hydrological and hydrometeorological case studies in Sect. 5.3.2 and Sect. 5.3.3, respectively.

5.3.1 Spatio-temporal correlations with ITSG-Grace2018 daily solutions

The temporal and spatial consistency of the TUD 5-day EWH grids is evaluated by comparing them with the independent ITSG-Grace2018 daily solutions, after applying a moving 5-day average to the latter. This validation considers both the "full" 5-day varying signal and the isolated sub-monthly variability obtained after removing the monthly mean, thereby assessing the ability of the proposed framework to recover high-frequency mass variations. Figure 12 summarises these comparisons: panel (a) shows the spatial correlation time series computed over the full latitude–longitude domain for both the complete signal and the sub-monthly residuals, while panels (b) and (c) present maps of temporal correlation computed independently for each grid cell for the full signal and sub-monthly residuals, respectively.

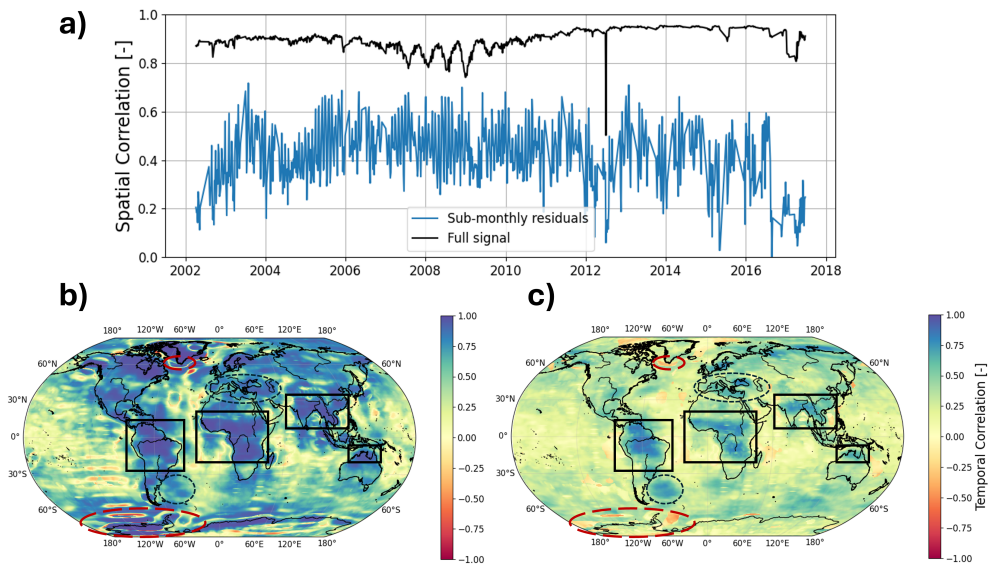


Fig. 12 Validation of the TUD 5-day hybrid solutions against 5-day moving-averaged ITSG-Grace2018 daily solutions. (a) Spatial correlation time series computed for each epoch over the full latitude–longitude domain for both the complete signal and the sub-monthly residuals. (b) Temporal correlation map for the full signal, computed independently for each grid cell. (c) Same as (b), but after removal of the monthly mean, isolating the sub-monthly variability. Major river basins, oceanic and shallow sea regions are outlined for reference.

Figure 12 demonstrates a strong agreement between the TUD 5-day hybrid and ITSG-Grace2018 daily solutions. For the full signal, the spatial correlation time series (Fig. 12a) exhibits consistently high values, with a mean correlation of 0.90, a maximum of 0.95, and a low standard deviation of only 0.04. The minimum correlation of approximately 0.50 occurs during a GRACE repeat resonance pattern in July 2012 and is associated with isolated along-track artefacts aligned with constant longitude bands, likely related to initial vector orbit mis-modelling in the Level-1B processing (see RMS of post-fit residuals in Fig. 5b). Overall, these statistics indicate a very high consistency in the combined monthly and sub-monthly variability captured by both solutions.

The temporal correlation map for the full signal (Fig. 12b) further confirms this agreement spatially. Over land, correlations generally range between 0.75 and 0.98, with the highest values (0.9–0.99), annotated in the figure, concentrated over major hydrological regions such as the Amazon, Ganges–Brahmaputra, and central African river basins. Oceanic regions typically exhibit slightly lower correlations of 0.6–0.9, although dynamically active regions such as the Zapiola Rise (highlighted by the circle in Fig. 12b) still reach correlations above 0.8. Globally, the temporal correlation statistics yield a median of 0.62, and a maximum approaching unity (0.998), with the comparatively large standard deviation of 0.30 primarily reflecting the strong spatial contrast between geophysically active and quiet regions.

For the isolated sub-monthly residuals (Fig. 12a,c), the correlations decrease substantially, as expected from the significantly smaller Signal-to-Noise Ratio, resulting from lower signal amplitudes and the increased relative contribution of noise and modelling differences. The temporal correlation map (Fig. 12c) reveals several localised artefacts with negative correlations, particularly south of Greenland (down to approximately -0.2) and along parts of the western Antarctic coastline. The Greenland feature is strongly associated with the side-lobe behaviour of the LGD and residual-range observables discussed in Sect. 5.2, while features over regions such as the Weddell Sea are linked to sharp spatial transitions in the weighting parameter α between the LGD- and range-dominated regimes (Fig. 11e). Similar decreases in correlation, occasionally reaching negative values, are also visible in the full-signal correlations (Fig. 12b), particularly along the north-western Antarctic coast.

Despite these localised artefacts, the sub-monthly residuals still exhibit substantial agreement (i.e. significant positive correlation) over geophysically active regions. The spatial correlation time series (Fig. 12a) shows a median correlation of 0.42 with a standard deviation of 0.14, and correlations ranging from approximately -0.01 to 0.72. Large land regions nevertheless maintain significant positive correlations of 0.6–0.75, particularly over the highlighted major river basins in Fig. 12c. The Amazon basin reaches correlations as high as 0.89, while the Indus and Ganges–Brahmaputra basins exhibit correlations of approximately 0.65–0.8. Similarly elevated correlations are also observed over the central African river basins, demonstrating that both datasets consistently capture part of the same sub-monthly hydrological variability. Enhanced sub-monthly agreement is additionally visible over several oceanic and hydrometeorological regions (annotated in Fig. 12a), including the Zapiola Rise (approximately 0.75–0.89), the Gulf of Carpentaria ($\sim$0.8), and parts of the Mediterranean and Black Seas (0.55–0.75). These spatial patterns closely match the global sub-monthly RMS variability previously identified independently in both the ITSG-Grace2018 daily solutions and the CSR RL06 post-fit residuals (Cuadrat-Grzybowski et al. 2025), further supporting the physical consistency of the retrieved 5-day mass anomalies. The comparatively reduced agreement over oceans and shallow seas is likely related to differences in ocean tide modelling between the CSR RL06 (Bettadpur 2018b) and ITSG-Grace2018 (Mayer-Gürr et al. 2018) processing chains, whose impact becomes increasingly important once the dominant monthly signal variability is removed.

5.3.2 High-frequency land hydrology: the 2007 Bangladesh floods

The 2007 flooding events in the Ganges–Brahmaputra river basin (Islam et al. 2010; Gouweleeuw et al. 2018) are analysed as a representative case of sub-monthly hydrological variability. Previous studies based on ITSG-Grace2018 daily solutions have identified pronounced flood-related signals in this region (Gouweleeuw et al. 2018; Retegui-Schiettekatte et al. 2025). In earlier work, we investigated the same events with a focus restricted to LGD post-fit residuals, analysed along-track and in the spatial domain (Cuadrat-Grzybowski et al. 2025). Here, we revisit that analysis using the novel methodology presented in this study.

Figure 13a shows that the TUD 5-day solutions clearly resolve three major flooding periods (annotated as (i)–(iii)). Period (i) is characterised by a nearly linear

increase in EWH throughout July, rising from approximately 0 to 10 cm over the course of the month, consistent with the reported extreme precipitation amounts of 500 to over 1000 mm (Islam et al. 2010). During period (ii), the variability decreases but two distinct flooding peaks are resolved in August, reaching EWH anomalies of approximately 10 cm and corresponding to renewed flooding episodes. Period (iii) represents the subsequent September flooding event, with peak EWH anomalies reaching approximately 13.5 cm, in agreement with renewed discharge peaks reported during this period (Islam et al. 2010). While the residual range-based formulation (blue curve) captures the overall sub-monthly variability relative to the monthly signal, it exhibits reduced spatial and temporal localisation of the individual flooding episodes: the two August peaks (Fig. 13a) are nearly indistinguishable. In contrast, the LGD and hybrid solutions (orange and red curves, respectively), as well as the ITSG-Grace2018 daily solutions, clearly resolve these individual events. This behaviour is expected and reflects the higher sensitivity of the range observable to low-frequency (low-degree) gravity signals compared to LGD, which provides improved localisation of mass anomalies (Ghobadi-Far et al. 2018).

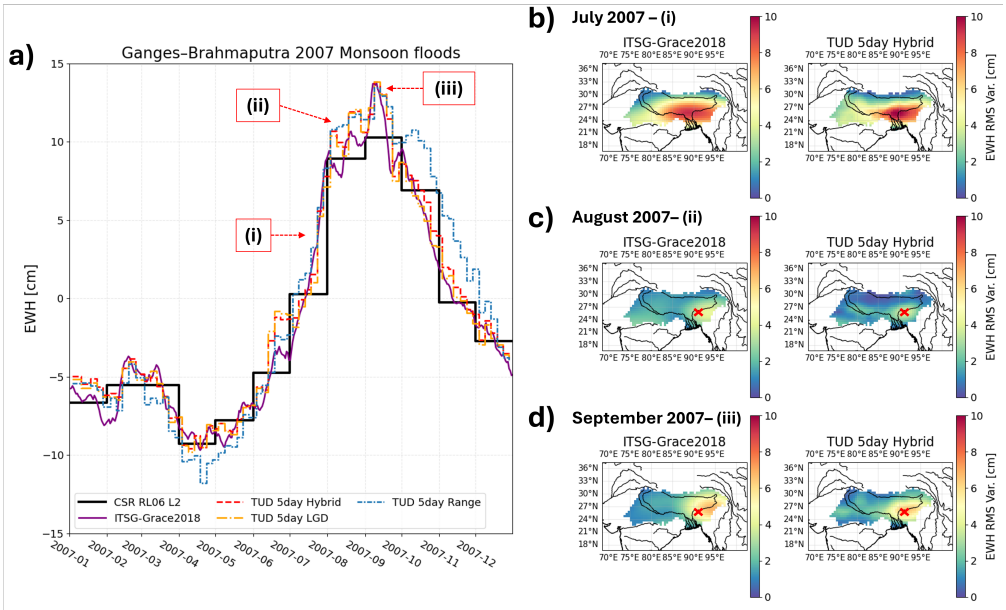


Fig. 13 Hydrological variability in the Ganges–Brahmaputra basin during 2007. (a) Basin-averaged EWH time series derived from TUD 5-day solutions (LGD, range, hybrid), compared with gently truncated monthly CSR RL06 solutions and ITSG-Grace2018 daily solutions. Three flooding events are indicated: (i) July, (ii) August, and (iii) September 2007. (b)–(d) Spatial distribution of sub-monthly EWH RMS variability for the three months: left panels show ITSG-Grace2018 daily solutions, and right panels show TUD 5-day hybrid solutions. Panels (b), (c), and (d) correspond to (i), (ii), and (iii), respectively. The red cross in panels (c) and (d) marks (25°N, 91°E).

The spatial distribution of the RMS sub-monthly variability of these events is shown in Fig. 13b–d. The ITSG-Grace2018 daily solutions (left column) capture the general structure of the flooding signal, but exhibit comparatively smoother and more spatially distributed patterns. In contrast, the TUD 5-day hybrid solutions (right panels) show a more concentrated representation of the sub-monthly variability, with enhanced signals occurring closer to the major river corridors. In particular, the variability associated with the Ganges river appears more pronounced along the western part of the river basin, while in eastern Bangladesh the enhanced variability is mainly confined to the southern and eastern sections of the Ganges–Brahmaputra delta region. This spatial concentration is less apparent in the daily solutions, where the corresponding anomalies appear more diffuse. This difference is particularly evident for the smaller peak on the 3rd of August and the larger September flooding event (Fig. 13a), where the TUD 5-day solutions show localised maxima near 25°N, 91°E (marked with a red cross in Fig. 13c,d), coinciding with regions reported to be affected by flooding (Islam et al. 2010; Cuadrat-Grzybowski et al. 2025). Given that no hydrological prior or temporal regularisation is imposed in the retrieval, the enhanced localisation suggests that this information is present in the GRACE observations and that the proposed methods can retrieve it more effectively.

Overall, while the ITSG-Grace2018 daily solutions provide high sub-monthly temporal information that is absent from the monthly solutions (Fig. 13a), their effective spatial resolution remains comparatively coarse (Gouweleeuw et al. 2018), owing to the truncation at spherical harmonic degree 40 (corresponding to an effective half-wavelength of approximately 500 km) and the additional DDK3 filtering. The isotropic component of the DDK3 filter has weights that decrease to 0.5 at an effective Gaussian radius of approximately 240 km (Kusche et al. 2009). In contrast, the TUD 5-day solutions recover the same temporal evolution while exhibiting more spatially localised mass anomaly patterns, thereby improving the delineation of sub-monthly signals without compromising their timing.

5.3.3 High-frequency hydrometeorology: Cyclone Oswald

A second example focuses on hydrometeorological variability associated with Cyclone Oswald in January 2013 (Bureau of Meteorology 2013; Deng and Ritchie 2020; Cuadrat-Grzybowski et al. 2025). Figure 14 summarises the temporal and spatial expression of this event, with (a) showing the region-averaged EWH time series over the Gulf of Carpentaria (17.5°S–11°S, 137.5°E–142.5°E), and (b)–(d) the corresponding spatial patterns of sub-monthly EWH RMS variability for December 2012, January 2013, and February 2013, respectively. In panels (b)–(d), ITSG-Grace2018 daily solutions (left) are compared with TUD 5-day hybrid solutions (right).

Figure 14a highlights the limitations of monthly CSR RL06 solutions in capturing sub-monthly variability. Due to temporal aliasing, the monthly averages (black curve) exhibit offsets of approximately 3–7 cm (notably between May and July 2013) with respect to both daily ITSG-Grace2018 (purple curve) and TUD 5-day solutions. In contrast, the sub-monthly solutions reveal pronounced peaks during January 2013, reaching 18–22 cm for ITSG-Grace2018, ∼15 cm for the TUD 5-day LGD and hybrid solutions, and ∼12 cm for the range-based solution, compared to a monthly mean

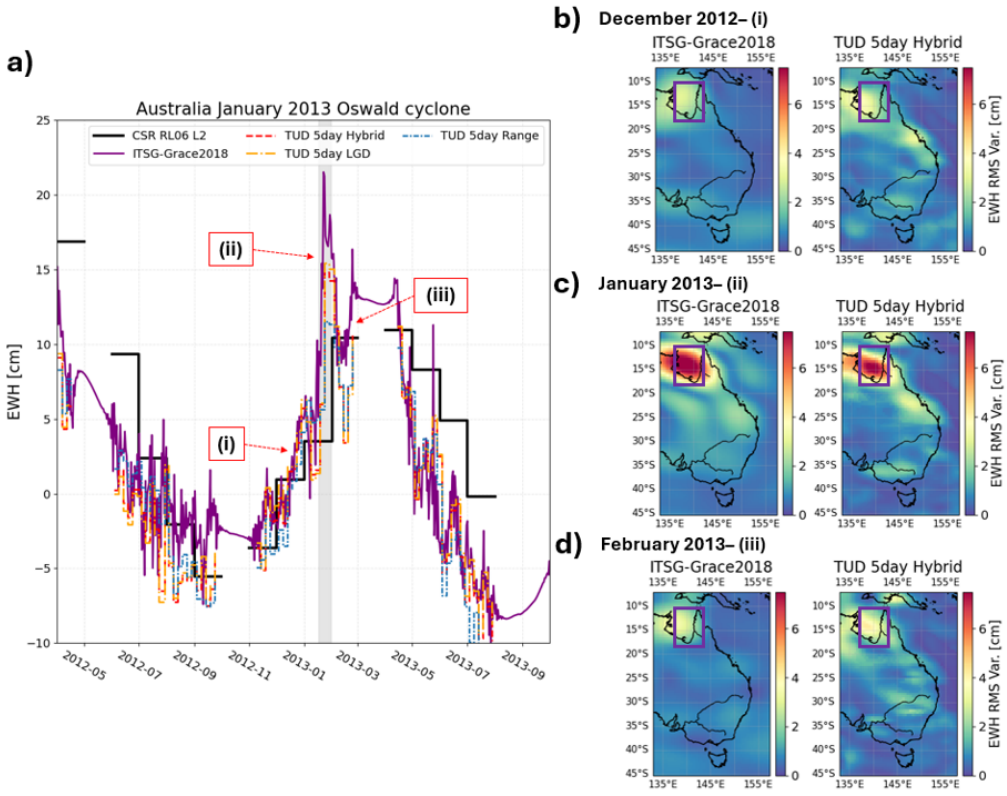


Fig. 14 Hydrometeorological variability in the Gulf of Carpentaria and north-western Australia associated with Cyclone Oswald (January 2013). (a) Region-averaged EWH time series derived from TUD 5-day solutions (LGD, range, hybrid), compared with gently truncated monthly CSR RL06 solutions and ITSG-Grace2018 daily solutions. Three periods are indicated: (i) December 2012, (ii) January 2013, and (iii) February 2013. (b)–(d) Spatial distribution of sub-monthly EWH RMS variability for the three periods, with ITSG-Grace2018 daily solutions shown in the left panels and TUD 5-day hybrid solutions in the right panels. Panels (b), (c), and (d) correspond to (i), (ii), and (iii), respectively. The period 17–29 January, corresponding to the passage of Cyclone Oswald, is highlighted in grey in panel (a). The averaging region (11°S–17.5°S, 137.5°E–142.5°E) is indicated in panels (b)–(d).

signal of ∼10 cm. These peaks occur within the duration of Cyclone Oswald, with two distinct maxima around 22–24 January, coinciding with the period of strongest pressure variations and precipitation (Deng and Ritchie 2020).

An additional feature is observed in the ITSG-Grace2018 daily time series (Fig. 14a), where periods without GRACE observations (e.g. May 2012, October 2012, March 2013, and August 2013) exhibit a smooth transition into adjacent months. This behaviour reflects the climatological constraint within the Kalman filtering approach, which enforces temporal continuity in the absence of observations (Kvas et al. 2019). As a result, the inherently more sporadic sub-monthly variability associated with hydrometeorological events is smoothed during these data gaps, whereas periods with

observations preserve the variability of the signals. In contrast, the TUD 5-day solutions contain gaps during these periods, as no observations are available to estimate the corresponding solutions. The spatial patterns (Fig. 14b–d) further support this interpretation. December 2012 and February 2013 (Fig. 14b,d) show relatively low variability of ∼4 cm, consistent with background mass fluctuations primarily driven by residual AOD and ocean tide signals (Ghobadi-Far et al. 2022).

In contrast, January 2013 (Fig. 14c) exhibits a marked increase in variability of approximately 7.5 cm, with a clear spatial concentration in the region of the cyclone's genesis (Bureau of Meteorology 2013). The TUD 5-day hybrid solutions closely reproduce the spatial extent and localisation of the cyclone-related mass variability observed in the ITSG-Grace2018 daily grids, while retaining a more spatially concentrated representation of the associated signal. This is particularly evident along the eastern coastline (Fig. 14b–d), where the January 2013 event exhibits enhanced variability of approximately 4.5 cm that follows the cyclone track (Bureau of Meteorology 2013; Deng and Ritchie 2020). In the TUD 5-day solutions, this coastal variability appears more clearly localised, whereas the ITSG-Grace2018 daily solutions exhibit a smoother spatial representation due to the characteristics of their Kalman-filtered estimation approach. In contrast, December 2012 and February 2013 show lower variability, of approximately ∼2.5 cm and ∼2 cm, respectively.

These results are consistent with Cuadrat-Grzybowski et al. (2025). The observed 7.5–8.5 cm EWH variability (Fig. 14c), converted into a spatially integrated mass anomaly, yields an estimated mass change of approximately 29–33 Gt within the study region for the TUD 5-day hybrid and daily solutions. The same event is identified in the LGD domain as a peak anomaly of -5 nm/s^2 on 21 January and -4 nm/s^2 on 22 January, corresponding to two consecutive GRACE ground tracks, as reported in that study. This behaviour was interpreted therein using a simple point-mass model assuming a constant 30 Gt perturbation (see Fig. 11 of that study).

5.4 Uncertainty characterisation of 5-day solutions

This section summarises the uncertainty characteristics of the LGD, range, and hybrid formulations of the 5-day EWH solutions (Sect. 5.4.1) and their increase relative to monthly Level-2 derived EWH grids (Sect. 5.4.2).

5.4.1 Propagated uncertainties across formulations

The uncertainty magnitude of the different 5-day formulations is assessed through the spatial and temporal characteristics of their regression- and observation-related uncertainty contributions. We limit ourselves to the "additional" uncertainties with respect to the monthly EWH component (all terms except the "L2" contribution in Eq. 37), as these are the only terms that vary between the different formulations introduced in this study, as summarised in Fig. 15. Panels (a)–(c) correspond to the hybrid, LGD, and residual-range formulations, respectively. For each case, subpanel (i) presents the global time series of the spatial RMedS of the uncertainty grids, separated into regression and KBR-related contributions (orange and blue curves, respectively)

together with the total uncertainty (black curve), while subpanel (ii) shows the spatial distribution of the temporal RMedS of the total uncertainty over the mission lifetime.

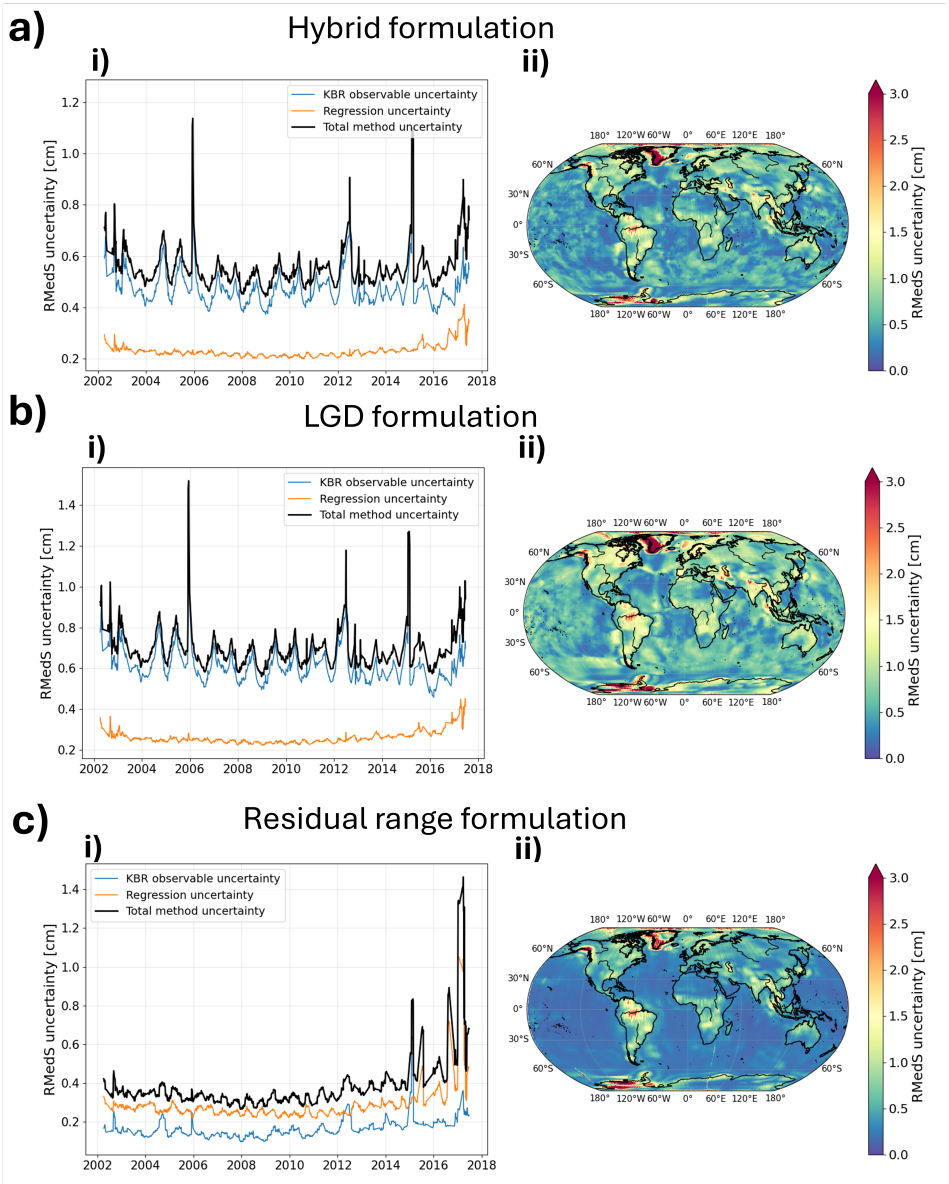


Fig. 15 Additional uncertainty components associated with the three formulations. (a) Hybrid, (b) LGD, and (c) residual range uncertainties. For each formulation, panel (i) shows the global time series of the spatial root median square (RMedS) of the uncertainty grids, separated into regression and KBR-related uncertainty contributions together with the total uncertainty. Panel (ii) shows the spatial distribution of the temporal RMedS of the total uncertainty grids over the full mission period.

For the LGD and hybrid formulations, the regression uncertainty component remains systematically smaller than the KBR-related uncertainty contribution (Fig. 15a(i),b(i)), with the latter exceeding the regression term by approximately a factor of 2–2.5. This behaviour reflects the stronger sensitivity of LGD-derived observables to observational transfer-function (Sect. 4.4) and correction-factor (Sect. 4.2) uncertainties, as well as the amplification of high-frequency KBR noise through differentiation, which is particularly visible in geophysically quiet regions such as the Sahara and over the oceans (Fig. 15b(ii)). In contrast, the residual-range formulation exhibits the opposite behaviour (Fig. 15c(i)), where the regression uncertainty becomes the dominant contribution, consistent with the comparatively lower instrumental noise level of residual range observations relative to their signal amplitude (see Table 5). The hybrid formulation additionally exhibits a reduced regression uncertainty by approximately 0.1–0.2 cm relative to both LGD and residual range (Fig. 15a(i)), which is expected from the optimisation of the weighting parameter α used to minimise the regression error (Sect. 3.5).

The main differences in the formulations are directly reflected in the total uncertainty levels (Fig. 15a(i)–c(i)). The LGD formulation exhibits the largest uncertainties overall, with a mean global uncertainty of 0.695 cm, values ranging from 0.559 to 1.519 cm, and a standard deviation of 0.102 cm (Fig. 15b(i)). Several pronounced peaks are visible during December 2005, July 2012, and January–February 2015, corresponding respectively to the GRACE satellite swap manoeuvre, during which the inter-satellite range temporarily decreased below 50 km and produced very large correction-factor values (Sect. 4.2), and to major resonance periods (McGirr et al. 2023) associated with strong post-fit residual outliers mapped into the 5-day spatial interpolation uncertainty of the KBR observables (Sect. 4.3.2). In contrast, the residual-range formulation (Fig. 15c) remains systematically lower, with a mean uncertainty of 0.375 cm, values between 0.265 and 1.463 cm, and a standard deviation of 0.138 cm (Fig. 15c(i)). Its temporal peaks are notably less pronounced, supporting the interpretation that the dominant LGD uncertainty amplification is primarily related to high-frequency noise introduced through differentiation. The main enhancements in the residual-range formulation occur during January–February 2015, July 2015, and from August 2016 onwards, the latter two being associated with reduced ground-track coverage and the one-accelerometer operational phase combined with battery degradation (McGirr et al. 2023), during which accelerometer noise increasingly contaminated the low-frequency spectrum to which residual range is most sensitive (Sect. 4.1). The hybrid formulation occupies an intermediate position, although remaining closer in magnitude to the LGD case due to the comparatively large transfer-function uncertainty contribution (Sect. 4.4), with a mean uncertainty of 0.553 cm, values between 0.441 and 1.137 cm, and a standard deviation of 0.084 cm (Fig. 15a(i)). Its temporal evolution closely follows the main LGD-related features, including the enhanced uncertainties during December 2005, July 2012, and January–February 2015, but with systematically reduced amplitudes of approximately 0.15 cm owing to the adaptive weighting between LGD and residual range through the parameter α.

The spatial uncertainty distributions (Fig. 15a(ii)–c(ii)) exhibit the same relative behaviour observed in the temporal statistics, with the LGD formulation showing the

highest uncertainty levels (global mean temporal RMedS of 0.825 cm and standard deviation of 0.684 cm), followed by the hybrid solution (0.659 cm and 0.530 cm), while the residual-range formulation remains systematically lower (0.502 cm and 0.540 cm). Elevated uncertainties are concentrated over regions of strong geophysical variability and enhanced transfer-function uncertainty, particularly major river basins and polar regions. Over most continental basins, LGD uncertainties reach approximately 1–1.5 cm, increasing to 1.5–3 cm over the Amazon and Ganges–Brahmaputra regions (Fig. 15b(ii)). In contrast, residual range generally exhibits lower land uncertainties of approximately 0.25–1 cm, although values still increase to 1–3 cm over the Amazon and 0.5–1.25 cm over the Ganges–Brahmaputra basin (Fig. 15c(ii)). The strongest uncertainties occur over the polar regions, where LGD reaches approximately 3–6 cm, the hybrid solution 3–5 cm, and residual range 2–3.5 cm (Fig. 15a(ii)–c(ii)), consistent with the enhanced transfer-function variability shown in Fig. 6. Although the residual-range formulation generally exhibits lower uncertainty, this does not necessarily imply superior performance. As demonstrated in Sect. 5.3.2 and Sect. 5.3.3, its greater sensitivity to low-frequency signals can limit the localisation of spatially constrained sub-monthly events. The hybrid formulation therefore provides a balance between the lower uncertainty of the range observable and the improved spatial localisation of LGD.

5.4.2 From monthly to 5-day solutions: uncertainty impact

We now assess the total uncertainty of the 5-day solutions, including the "L2" contribution, in order to quantify how much additional uncertainty is introduced by increasing the temporal resolution from monthly EWH grids to 5-day solutions. We limit the analysis to the hybrid formulation for brevity, as the relative uncertainty behaviour between the LGD, residual-range, and hybrid formulations was already characterised in Sect. 5.4.1. Figure 16 summarises the relative increase in total uncertainty of the 5-day hybrid solution with respect to the monthly EWH grids. The metric is defined as the relative difference between the spatial RMS of the 5-day total uncertainty and the spatial RMS of the corresponding monthly EWH uncertainty (derived from Level-2 solutions), computed separately over land and ocean regions:

$$\left(\frac{\mathrm{RMS}\left\{\sigma_{h,\mathrm{5d}}\right\}}{\mathrm{RMS}\left\{\sigma_{h,\mathrm{L2}}\right\}} - 1 \right) \times 100 \ [\%].$$

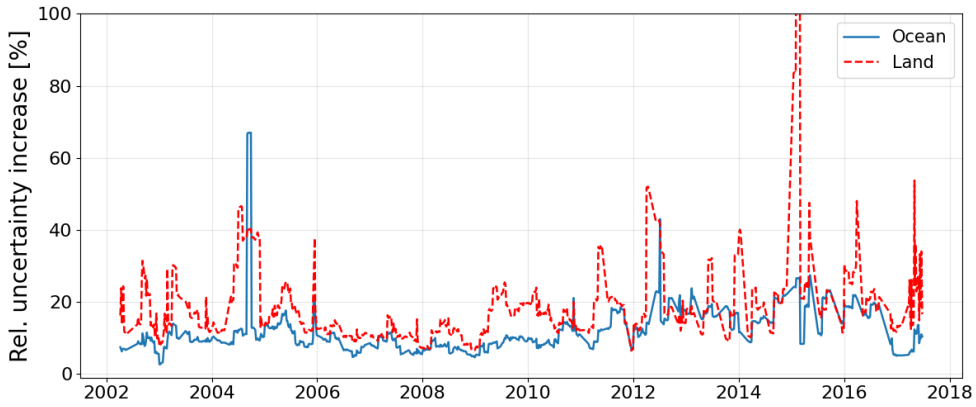


Fig. 16 Time series of the relative increase in total uncertainty of the TUD 5-day hybrid solutions with respect to the monthly EWH uncertainty grids. The metric is computed as the relative RMS increase of the total uncertainty between the 5-day and monthly solutions, evaluated separately over land and ocean regions.

Over oceans (solid blue curve), the increase remains comparatively limited, with a full-mission mean of 11.8% (median of 10.0%), and a robust standard deviation (see Sect. 3.3.4) of 4.1%. The most stable behaviour occurs during the 2005–2010 period, where the mean increase reduces to approximately 9.0% (8.5% median) with a standard deviation of only 2.8%. In contrast, the 2011–2017 period exhibits a larger mean increase of 15.4%, consistent with the lower quality of GRACE observations (i.e. one accelerometer was turned off due to battery degradation) during the later mission years as discussed previously (Sect. 5.4.1). The largest oceanic increase reaches approximately 67% during September 2004, coinciding with a resonance period.

Over land (red dashed curve), the relative uncertainty increase is systematically larger, reflecting the influence of signal geophysical variability into the spatial interpolation error components (Sect. 4.3.2) and the increased sensitivity of the transfer function over polar regions (Sect. 4.4). For the full mission, the mean increase reaches 18.9% with a median of 16.3%, while the robust standard deviation remains comparatively moderate at 6.7%, indicating that the majority of epochs remain well constrained despite several isolated outlier periods. The most stable interval again corresponds to 2005–2010, with a mean increase of 14.0% and a standard deviation of 4.7%. Larger increases are observed during both the early mission phase (2002–2004; mean of 21.3%) and particularly the late mission years (2011–2017; mean of 23.6%), where the larger variability and extreme values are associated with the same resonance and instrumental effects identified in the uncertainty time-series analysis (Sect. 5.4.1). The maximum land increase reaches approximately 134% during the strongest resonance period of February 2015.

Overall, these results demonstrate that the increase in uncertainty associated with the transition from monthly to 5-day solutions remains comparatively moderate given the six-fold increase in temporal sampling. Under a simple white-noise averaging

assumption and assuming the same spectral truncation, one would expect an amplification of approximately $\sqrt{30/5} \approx 2.45$, i.e., about 145% for nominal conditions without additional regularisation. In unconstrained settings, and particularly during periods of reduced ground-track coverage or resonance repeat cycles, one would further expect this effect to be amplified. These conditions are indeed where the largest increases are observed in our 5-day solutions. In contrast, over most of the mission, the observed increase remains substantially lower. The strongest uncertainty amplification is concentrated over geophysically active continental regions, whereas oceanic regions remain comparatively stable throughout most of the mission lifetime. This confirms that the proposed framework preserves much of the stability of the original monthly Level-2 solutions while enabling substantially enhanced temporal resolution.

5.5 Temporal consistency of 5-day solutions

The proposed high-frequency framework relies on residual Level-1B products generated within the standard monthly GRACE Level-1B to Level-2 processing chain. Consequently, although sub-monthly variability is recovered (see Sect. 5.3) from the residual observations, both the geo-fit and post-fit residual components remain tied to the monthly gravity field recovery process (Pini 2012). Assessing the temporal consistency of the resulting 5-day EWH grids is therefore essential to identify potential discontinuities associated with this pre-defined monthly partitioning. The consistency is evaluated through consecutive differences between neighbouring 5-day EWH grids, denoted as ΔEWH. The analysis considers both the internal consistency within individual months and the behaviour across month boundaries. For brevity, only the hybrid formulation is considered, as the corresponding results for the LGD- and range-based formulations are similar.

Figure 17 summarises the diagnostics using the RMedS, which reduces the influence of isolated resonance and repeat-pattern artefacts. Panel (a) shows the global spatial RMedS time series of consecutive differences for both intra-month and inter-month transitions, together with the corresponding histograms. Panels (b) and (c) show the temporal RMedS maps of intra-month and inter-month consecutive differences, respectively, with selected regions of interest highlighted.

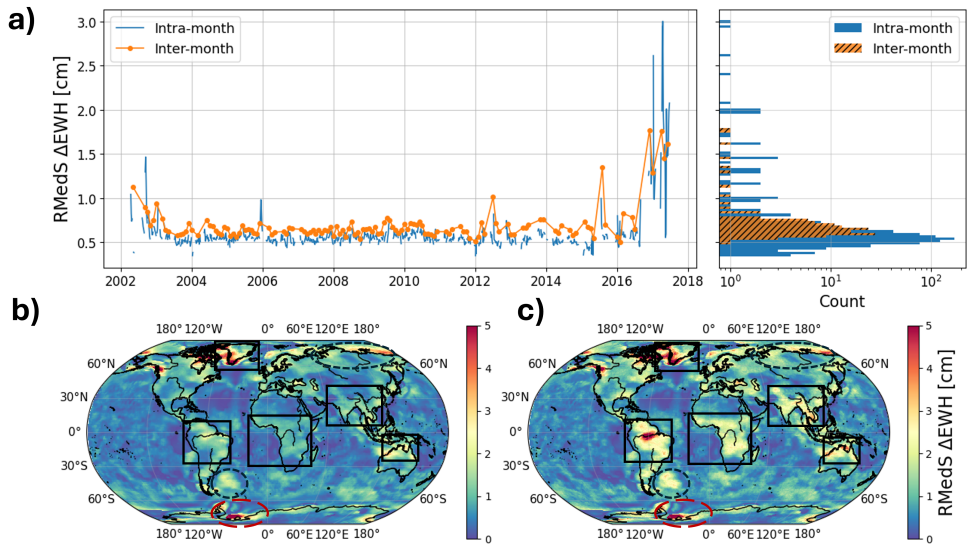


Fig. 17 Temporal consistency diagnostics of the TUD 5-day hybrid solutions based on consecutive 5-day EWH differences. (a) Global spatial RMedS time series of consecutive intra-month and inter-month differences, together with their corresponding histograms. (b) Temporal RMedS of intra-month consecutive differences. (c) Same as (b), but for inter-month consecutive differences. Selected hydrological, hydrometeorological, and oceanic regions are highlighted for reference.

The global statistics in Fig. 17a indicate that inter-month consecutive differences are, on average, approximately 0.2 cm larger than intra-month differences. Nevertheless, the intra-month differences exhibit both higher maxima (above 2 cm, compared to approximately 1.75 cm for inter-month transitions) and lower minima (∼0.35 cm versus ∼0.5 cm). This behaviour is primarily attributed to the higher sensitivity of the spatially interpolated 5-day post-fit residuals to isolated outliers, in particular those related to initial state vector mis-modelling and accelerometer-related disturbances, which locally amplify consecutive differences. In contrast, the inter-month behaviour is more strongly controlled by the monthly geo-fit component near month boundaries relative to the interpolated 5-day post-fit residuals (Sect. 3.2.1).

The spatial diagnostics (Fig. 17b,c) further demonstrate that the increase in inter-month variability is strongly region-dependent. Over major hydrological regions, the inter-month RMedS is typically at least twice as large as the intra-month values. This behaviour is particularly evident over the Amazon basin, where the RMedS increases from a maximum of approximately 2.5 cm for intra-month differences (Fig. 17b) to nearly 5-6 cm for inter-month transitions (Fig. 17c). The Zapiola Rise similarly shows an increase by a factor of approximately 1.5 between intra- and inter-month differences. In contrast, hydrometeorological regions over northern Australia exhibit comparatively small differences between both diagnostics, typically within a factor of 1–1.25. Regions such as northern Russia and Greenland show similar variability levels in both cases, generally between 3 and 5 cm. An additional artefact is visible in the Weddell Sea and

along parts of the western Antarctic coastline (highlighted by dashed red contours in Fig. 17b,c). These features are associated with sharp spatial transitions in the hybrid weighting parameter α, producing localised discontinuities between LGD- and range-dominated regimes (see Fig. 11e).

Importantly, the observed differences between intra- and inter-month consecutive 5-day grids represent a methodological feature of the current processing strategy rather than a loss of geophysical information. We hypothesise that these discontinuities originate primarily from the monthly estimation framework of the Level-1B processing, where the local and common fit parameters (see Eq. 1 in Cuadrat-Grzybowski et al. (2025)) are estimated independently for each monthly solution. Consequently, month-dependent common fit parameters, as well as potential differences in the local fit parameters as described by Pini (2012) associated with the first and last arcs of consecutive months, may introduce discontinuities at month boundaries.

Nevertheless, these discontinuities remain smaller than the natural differences between independent monthly gravity-field solutions. Comparing with the month-to-month variations derived directly from the geo-fit component shows that the inter-month differences in the 5-day solutions are smaller by approximately a factor of 2–5 compared to the corresponding geo-fit month-to-month variations (not shown). This highlights the added value of combining monthly geo-fits with sub-monthly residuals, as the resulting 5-day solutions provide improved temporal continuity across months, compared to the monthly solutions themselves. Furthermore, the underlying sub-monthly signal remains coherent, as demonstrated through independent validation against ITSG-Grace2018 daily solutions (Sect. 5.3.1), where high spatial and temporal correlations are observed across the same variability patterns, and through the application to selected sub-monthly hydrological and hydrometeorological case studies (Sect. 5.3.2 and Sect. 5.3.3).

6 Conclusions and Recommendations

6.1 Summary and conclusions

We present a fully data-driven framework to transform residual GRACE Level-1B ranging observables into global 5-day gravity-field solutions expressed as EWH grids. The proposed approach establishes, for the first time, an empirical and spatially distributed relationship between residual KBR/LRI-type observables (i.e., residual LGDs and ranges) and mass anomalies expressed in EWH. The resulting spatially varying regression parameters provide a direct transformation between instantaneous ranging observables and EWH, enabling their use for high-frequency mass change estimation without requiring access to Level-2 gravity field solutions.

A key finding of this study is that the observable-to-EWH relationship is neither spatially nor temporally constant. Instead, the empirical mapping depends on both the amplitude of the underlying mass signal and the instantaneous orbital configuration of the GRACE satellites. We demonstrate that variations in inter-satellite range and orbital altitude introduce systematic amplitude changes in the ranging observables, requiring an explicit altitude- and range-dependent correction factor. Without this

correction, changes in the GRACE orbital configuration translate directly into spurious variations in the derived EWH grids. Accounting for these dependencies enables consistent retrieval of the monthly gravity-field signal and its sub-monthly variability from residual Level-1B observations.

An additional outcome of this work is the provision of spatially distributed uncertainty estimates for every product formulation (LGD-, range-, and hybrid-based solutions). These uncertainty grids are propagated directly from the observational uncertainties, interpolation procedures, empirical correction factors, regression model, and Level-2 reference fields. This enables the resulting 5-day EWH solutions to be directly used in applications requiring physically consistent error characterisation, such as hydrological data assimilation. On average, the additional uncertainty introduced by the 5-day sampling remains moderate, increasing by approximately 12% over oceans and 18% over land relative to monthly EWH grids derived from Level-2 data. This increase is substantially lower than the factor of approximately $\sqrt{30/5} \approx 2.45$, corresponding to a 145% increase, expected from an unconstrained reduction of the temporal averaging window based purely on statistical averaging assumptions.

The recovered high-frequency mass variability is demonstrated through a spatio-temporal correlation comparison with independent ITSG-Grace2018 daily solutions. For the full signal, temporal correlations exceed 0.9 and reach values up to 0.99, while spatial correlations are typically between 0.8 and 0.9. After removing the monthly mean, the retrieved sub-monthly variability remains coherent, with temporal correlations of 0.6–0.8 over major river basins, approximately 0.7 over shallow seas, and above 0.75 over the Zapiola Rise. The solutions remain consistent during challenging orbital configurations, including the December 2005 GRACE satellite swap manoeuvre.

The added value of the 5-day solutions is further demonstrated through geophysical applications. The 2007 Bangladesh monsoon flooding and the January 2013 Cyclone Oswald event reveal temporal evolution that is not resolved by monthly products, while remaining consistent with the daily solutions' variability where available. These examples highlight the capability of the proposed framework to capture sub-monthly hydrological and hydrometeorological mass variations without relying on external geophysical constraints.

Finally, compared to existing approaches based on temporal regularisation, Kalman filtering, or geophysical background models, the proposed methodology is entirely data-driven. It does not impose temporal correlations or external geophysical priors. The only a priori information entering the processing is the reference background force model required to generate the pre-fit residuals, which is a standard and necessary step in Level-1B processing. The proposed framework instead exploits the information contained in the resulting Level-1B residual observations and the conventional Level-1B to Level-2 processing chain. Consequently, it can be applied to standard GRACE/GRACE-FO residual observations generated by existing processing centres, providing an accessible pathway for deriving high-frequency gravity field estimates from current and future satellite gravimetry missions.

The resulting dataset is provided as the TUD-L3Uncorr-5dayEWH(_UNC) product (Cuadrat-Grzybowski et al. 2026b), including both EWH and associated uncertainty grids, thereby providing all information required for direct use in data assimilation frameworks.

6.2 Recommendations

Future improvements should focus on the recovery of low-degree spherical harmonic content (below degree 5), which is partially attenuated by the temporal filtering inherent in the residual Level-1B processing. In addition, filtering choices in monthly EWH reconstruction require careful consideration, as the LGD-to-EWH transformation introduces amplitude-dependent effects comparable to DDK3-level smoothing. It is further noted that the present products do not include corrections for GIA or geocentre motion, and still contain residual tidal aliasing effects, which should be accounted for in applications targeting climatological studies.

Finally, the altitude and range correction strategy should be further refined. In particular, the present formulation assumes effective constant correction coefficients, whereas the results indicate that these factors are themselves functions of orbital geometry, and in particular of altitude. Developing a non-constant, altitude-dependent correction model is therefore a key avenue for improving the method across different orbital regimes. Additionally, the monthly estimation framework of the underlying Level-1B processing should be investigated to mitigate the small discontinuities observed between consecutive monthly solutions. These discontinuities are likely related to the independent estimation of monthly local and common parameters (Pini 2012), which we hypothesise introduce month-dependent offsets and differences between adjacent arc solutions. Future approaches could therefore investigate alternative treatments of the sub-monthly adjustment (from post-fit residuals) to improve the temporal consistency across month boundaries.

Acknowledgements. We thank Jose van den IJssel (TU Delft) for valuable discussions that helped shape the conceptual and methodological aspects of this work. Last but not least, we thank the Center for Space Research (CSR) for making the Geofit and Postfit dataset publicly available. This research would not have been possible without these data.

Declarations

Funding

Frederik Jacobs is supported by the Dutch Research Council (NWO) as part of the project *Relative acceleration modelling (RAM)* with file number *ENW.GO.002.002* of the research programme *Use of space infrastructure for Earth observation and planetary research.*

Conflict of interest / Competing interests

The authors declare that they have no competing interests.

Ethics approval and consent to participate

Not applicable.

Consent for publication

Not applicable.

Data availability

The datasets used in this study are publicly available and consist of Level-1B GRACE/GRACE-FO residual products, Level-2 spherical harmonic (SH) solutions, and derived equivalent water height (EWH) products.

The three versions of the uncorrected 5-day Level-3 GRACE equivalent water height solutions (LGD, Hybrid, and Range) are available from the TU Delft GRACE-Cube repository: https://grace-cube.lr.tudelft.nl/L2B_5DAY/v2.0/ with associated DOI: https://doi.org/10.4121/a685e7cf-1b84-4007-b206-89ae1c71dd6c.

The underlying CSR Level-1B residual data used in the processing chain are available at: https://doi.org/10.18738/T8/VY3U8L.

Level-2 SH gravity field solutions used for comparison and consistency checks are publicly available through the International Centre for Global Earth Models (ICGEM) database: https://icgem.gfz-potsdam.de/.

Materials availability

Not applicable.

Code availability

All Level-2 Spherical Harmonic products were converted to equivalent water height using l3py software (Kvas 2018) and standard spherical harmonic synthesis and filtering procedures described in the methodology section of this study.

AI usage statement

Portions of this manuscript were edited using ChatGPT (OpenAI) and Grammarly to improve grammar, sentence structure, and clarity of expression. The scientific content, analyses, interpretations, and conclusions are entirely the responsibility of the authors.

Author contributions

M. Cuadrat-Grzybowski: Conceptualisation, methodology, software, validation, formal analysis, investigation, data curation, visualisation, writing – original draft, writing – review and editing.

J. Teixeira da E.: Conceptualisation, methodology, supervision, writing – review and editing.

F. Jacobs: Conceptualisation, methodology related to the altitude- and range-correction approach, writing – review and editing.

P. N. A. M. Visser: Conceptualisation, supervision, writing – review and editing.

A Filtering choices for spherical harmonic coefficient synthesis

To assess the sensitivity of the temporal correlations to the filtering parameters applied during spherical harmonic synthesis, we evaluated different DDK filter strengths and gentle truncator upper degree limits (l_b; Sect. 2.3). The Pearson temporal correlation coefficient, computed between the time series of each grid cell, was used as the primary performance metric. Specifically, correlations were evaluated between the LGD and range-based observables and the corresponding equivalent water height (EWH) grids synthesised from the monthly Level-2 spherical harmonic solutions.

Based on previous studies (e.g., Werth et al. 2009; Güntner et al. 2024; Qian et al. 2022; Li et al. 2025a), filters DDK3–DDK5 were selected for the main analysis, as lower levels (DDK1–DDK2) are known to cause excessive attenuation and geophysical signal distortion in high-variability regions such as Greenland and Antarctica. The

lower truncation limit was fixed to $l_a = 2$, which ensures that the dominant degree-2 components (with corresponding frequencies below ∼0.35 mHz for GRACE) are excluded, which is consistent with the temporal frequency filtering applied to the (range rate) geo-fit time series (Sect. 3.1).

To motivate the choice of the upper truncation limits $l_b = 3$–7, we consider the approximate correspondence between temporal frequency and spherical harmonic degree for a circular orbit:

$$f \approx l \frac{1}{\pi R} \sqrt{\frac{GM}{R+h}}, \tag{38}$$

where R is the mean Earth radius (6371 km), GM is the Earth's gravitational parameter, and h is the satellite orbital altitude. As shown in Fig. 18, for GRACE mean altitudes (350–550 km), a temporal frequency of $f \approx 0.9$ mHz maps to approximately degree $l \approx 5$. This is the frequency band retained by the temporal filtering applied to the geo-fit time series, so the spatial truncation should preserve the corresponding spectral content as closely as possible. Choosing l_b between 3 and 7 therefore brackets the degree associated with $f \approx 0.9$ mHz while allowing a controlled sensitivity analysis around this dominant contribution. The weak dependence of this mapping on mean altitude is also illustrated in Fig. 18.

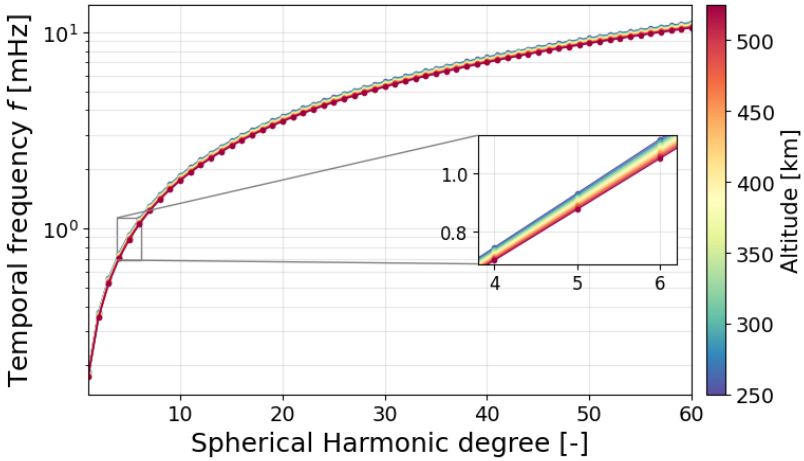


Fig. 18 Approximate relationship between temporal frequency and spherical harmonic degree assuming a circular orbit. Curves are shown for different mean altitudes (250 to 550 km). A frequency of $f = 0.9$ mHz corresponds approximately to degree $l \approx 5$. The inset zoom (degrees 4–6) illustrates the weak sensitivity to mean altitude variations.

Fig. 19 summarises the results of this brief analysis. Panels (a,b) present temporal correlation statistics for LGDs and panels (c,d) show the same diagnostics for residual range; panels (a,c) vary the DDK filter level while keeping l_b fixed, and panels (b,d) vary l_b while keeping DDK fixed. Note that negative correlations are expected between LGDs and EWHs, reflecting that a positive mass anomaly produces a negative peak

in the residual LGD signal, whereas positive correlations are expected for ranges and EWHs, consistent with a positive peak residual range for a positive mass anomaly.

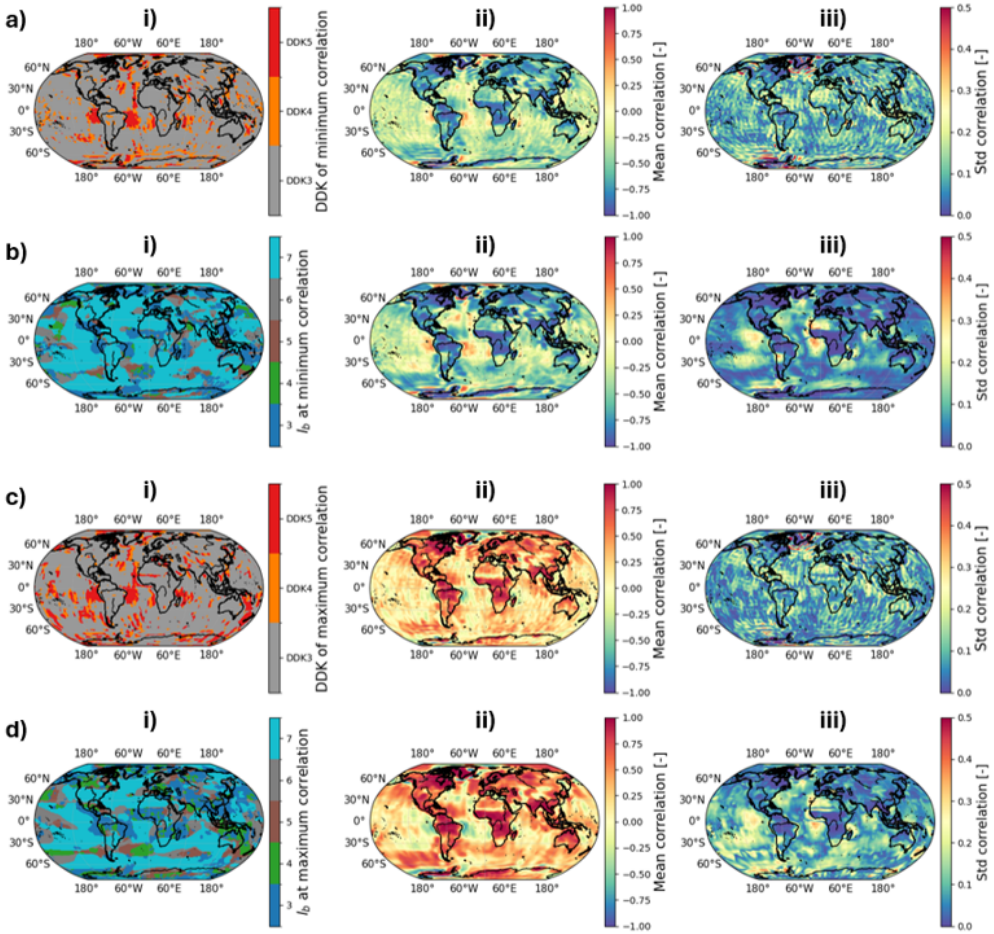


Fig. 19 Temporal correlation (period: July 2003 - August 2016) statistics between monthly gridded LGDs (a, b) and range (c, d) with EWH grids derived from Level-2 solutions. Panels (a,c) show results for a fixed truncation degree of $l_b = 7$ while varying the DDK filter level from 4 to 5. Panels (b,d) show results for a fixed DDK3 filter while varying l_b between 3 and 7. For each case, (i) indicates the DDK or l_b value corresponding to the minimum (LGD) or maximum (range) correlation, and (ii)–(iii) show the mean and standard deviation of the correlation across all tested filters or l_b values.

From Fig. 19, $l_b = 7$ emerges as the best compromise: it tends to maximise (anti-)correlation (see panels b,d(i)) while preserving low-frequency geophysical signal and shows only small variability across major river basins (see standard deviation typically smaller than 0.1; panels b,d(iii)). By contrast, the correlation metric is substantially more sensitive to the choice of DDK filter: panels a,c(iii) show global

standard-deviation values on the order of 0.1–0.3, with the largest problems (standard deviations above 0.5) confined to transitional and high-gradient regions (e.g., coastal transition zones and icy regions such as parts of Greenland and Antarctica). The strongest unfiltered high-frequency noise, manifested as striping, appears predominantly for the weakest smoothing (DDK5, and to a lesser extent DDK4), whereas DDK3 exhibits the most spatially extensive (anti-)correlation, reflected by the predominance of gray-shaded regions in panels a,c(i).

In conclusion, the combination of DDK3 filtering and $l_b = 7$ gentle truncation is adopted for the main analysis as the optimal balance between suppressing noise and preserving the spatial distribution. Nevertheless, future work will investigate this filter–truncation trade-off more systematically at the monthly level, to better characterise how the LGD and range observables relate to monthly EWH grids under varying temporal and spectral resolutions.

B Additional information related to spatial interpolation

This appendix provides complementary details to Sect. 4.3.2, focusing on the temporal characteristics of the 5-day interpolation absolute error and the choice of scaling estimator. In particular, it motivates the use of the *Root Median Square* (RMedS) instead of the conventional RMS when defining the scaling metric. The RMedS is adopted to reduce the influence of mis-modelled initial state vector signatures that are unintentionally absorbed into the geo-fits during the estimation process (see Sect. 2.1) but are absent from the corresponding post-fit residuals.

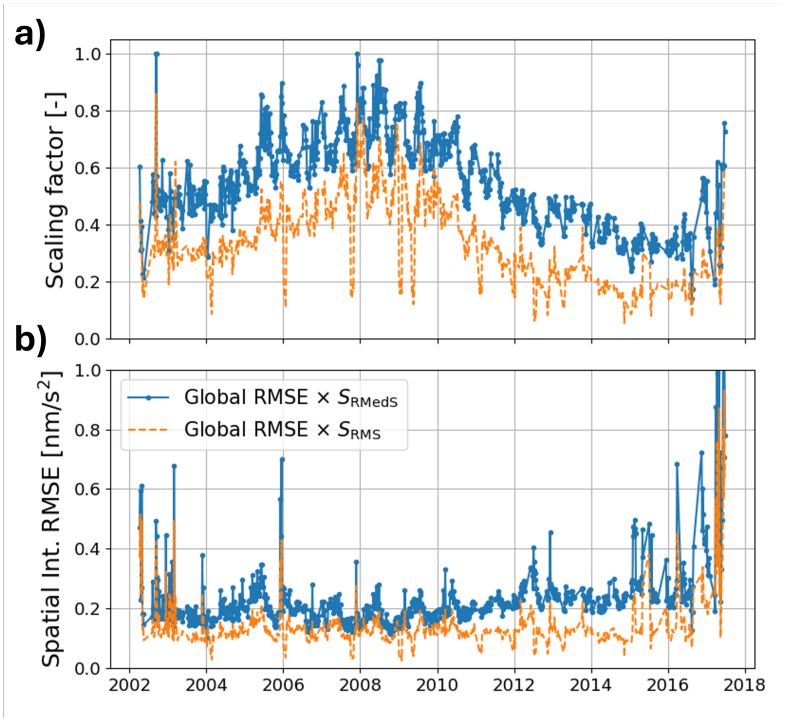


Fig. 20 Temporal and spatial characteristics of the direct spatial interpolation error in the case of 5-day sets of Line-of-Sight Gravity Differences. **(a)** Scaling factor S derived from both the RMS and RMedS (Root Median Square) estimators, **(b)** global RMS of the 5-day spatial interpolation error time using the RMS and RMedS estimators.

The global RMS of the simulated interpolation error, $\sigma_{5\mathrm{d,int}}^{(\mathrm{sim.geo\text{-}fit})}$ (bold black curve in Fig. 5b; see main text), exhibits a clear "V-shape" over time, with a maximum around January 2008, corresponding to the GGM05C reference epoch. This shape arises because the monthly fields are expressed as anomalies with respect to GGM05C, while the global geophysical signal is dominated by the nearly linear ice-sheet-mass-loss trend. When this trend is squared in the RMS, values increase with distance from the reference epoch on both sides, producing the observed V-shape. Since we aim to isolate the actual interpolation error rather than preserve this signal-driven temporal pattern, the scaling factor should not reproduce the V-shape as is.

When S_R is computed using the RMS, the resulting curve (orange dashed line in Fig. 20a) shows only a weaker V-shape, with flatter lower branches and unrealistically low peaks (below 0.2). This indicates that the RMS formulation is more affected by outliers in the geo-fit signal power and is therefore less robust. In contrast, the RMedS-based scaling factor (blue dot–dash curve) follows the temporal evolution more consistently (Fig. 20b) while reducing the influence of outliers. As a result, the RMedS estimate is more conservative, yielding scaling factors that are on average about twice as large as those obtained with the RMS. For these reasons, the RMedS formulation is adopted as the robust estimator for scaling the 5-day interpolation uncertainty.

C Analytical estimation of altitude power law rule

This appendix provides an analytical estimate of the altitude-dependent scaling exponent, n_r, used to correct observables for orbital height differences. The derivation is based on spectral representations of the signal and aims to explain the empirically observed power-law behaviour. This analysis is consistent with the analytical expressions derived by Kim (2000).

C.1 Residual gravity difference

We begin from the standard deviation per spherical harmonic degree l of the gravitational potential, denoted σ_l^V. Using Kaula's rule, the degree-wise standard deviation follows (Kim 2000):

$$\sigma_l^V \propto \sqrt{\frac{2l+1}{l^4}}. \tag{39}$$

The gravity anomaly at altitude r is obtained through differentiation and upward continuation, giving the Kaula-type amplitude scaling:

$$\sigma_l^{\delta g}(r) \propto (l+1)\sqrt{\frac{2l+1}{l^4}}\left(\frac{R}{r}\right)^{l+1}. \tag{40}$$

Assuming an empirical power-law representation of the LGD, $\delta g_{||}$,

$$\frac{\delta g_{||}^{\mathrm{ref}}}{\delta g_{||}} \approx \left(\frac{r}{r_{\mathrm{ref}}}\right)^{n_r}, \tag{41}$$

the effective exponent n_r is defined from the ratio of spectral amplitudes:

$$\left(\frac{r}{r_{\mathrm{ref}}}\right)^{n_r} \approx \frac{\sum_{l=l_{\min}}^{l_{\max}}(l+1)\sqrt{\frac{2l+1}{l^4}}\left(\frac{R}{r_{\mathrm{ref}}}\right)^{l+1}}{\sum_{l=l_{\min}}^{l_{\max}}(l+1)\sqrt{\frac{2l+1}{l^4}}\left(\frac{R}{r}\right)^{l+1}}. \tag{42}$$

This formulation shows that n_r depends on orbital altitude h (via $r = R + h$) and on the minimum spherical harmonic degree $l_{\min}$. The influence of $l_{\max}$ (typically 54–60) is negligible and is omitted for brevity.

C.2 Residual range formulation

Following Kim (2000), the variance of the range-rate observable is related to the Kaula-type spectral representation of the gravitational potential through a degree-wise scaling in spherical harmonics. To obtain the corresponding residual range formulation, a single temporal integration is introduced in the frequency domain via the factor $(2\pi f)^{-1}$. The Kaula-consistent standard deviation of the residual range at orbital

radius r is therefore written as:

$$\sigma_l^{\delta\rho}(r) \propto \frac{1}{2\pi f}\sqrt{1 - P_l(\cos\theta)}\sqrt{\frac{2l+1}{l^4}}\left(\frac{R}{r}\right)^{l+1/2}, \tag{43}$$

where P_l is the Legendre polynomial evaluated at the inter-satellite angle θ. A mapping between temporal frequency f and spherical harmonic degree l is assumed following Eq. 38. Furthermore, for a typical GRACE altitude and inter-satellite range of 450 km and 220 km, respectively, and assuming a circular orbit, the angle is approximately given by $\theta \approx \arcsin(\rho/r) \approx 1.9°$. Over the full range of realistic GRACE altitude and inter-satellite distance variations, the corresponding changes in $\cos(\theta)$ remain extremely small (of the order of the fourth decimal place around $\cos(\theta) \approx 0.999$), resulting in a negligible impact on the term $P_l(\cos\theta)$. Consequently, θ is approximated as a constant value of 2°, consistent with Kim (2000).

Lastly, the corresponding spectral representation of the residual range is then obtained by inserting this expression into the degree-wise summation used for the altitude scaling analysis (Eq. 42).

C.3 Results

As a first analysis, we investigate how the effective scaling exponent n_r for LGD and residual range depends on the satellite altitude ratio h/h_{ref} and the minimum degree l_{min}. Figure 21 shows n_r as a function of the normalised altitude, for $l_{\text{min}} = 4, 5, 6$, with $h_{\text{ref}} = 450$ km.

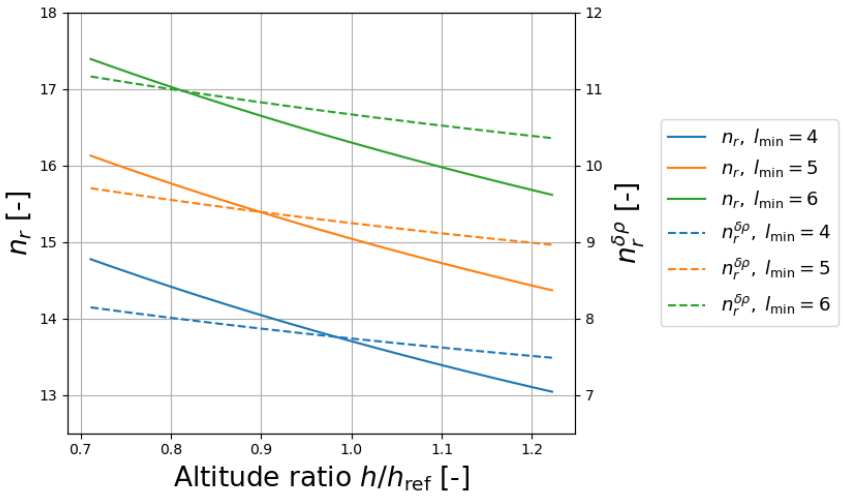


Fig. 21 Altitude scaling exponent n_r as a function of normalised altitude h/h_{ref} for LGD (solid lines) and residual range (dashed lines) for three different l_{min} (4, 5, and 6). Lower l_{min} corresponds to inclusion of longer-wavelength components.

As expected, decreasing $l_{\min}$, i.e., including longer-wavelength components in the gravity field, reduces the required scaling coefficients for both observables, with a slope of approximately 1.5 per degree. While this slope is similar for LGD and residual range in terms of the minimum degree, the altitude sensitivity is different: LGD exhibits a variation in n_r over the considered orbital range that is roughly double that of the residual range, reflecting the residual range's weaker dependence on orbital altitude.

Using GRACE-like orbital altitudes in the range 320–550 km, with $l_{\max} = 60$ and a reference altitude $h_{\text{ref}} = 450$ km, the statistical results for n_r for $l_{\min} = 5$ are summarised in Table 7. These results show that the effective scaling for LGD and for residual range can be assumed to be constant (relative standard deviations are below 3.5%), supporting the power-law correction approach described in Sect. 3.3.

Table 7 Analytical estimate of the altitude scaling exponent n_r for residual gravity difference and residual range over the GRACE altitude range (320–550 km) with $l_{\min} = 5$.

Observable	Mean n_r	Std. dev.
Residual gravity difference	15.184	0.507
Residual range	9.305	0.213

D Simulation-based estimation of altitude power law rule

This appendix summarises the simulation-based estimation of the altitude power-law exponent n_r and the verification of the constant-exponent assumption using synthetic GRACE-like scenarios.

D.1 Population of estimates

The population of n_r estimates is generated from the suite of synthetic experiments described in Sect. 3.3. For each pair of simulation cases with different initial orbital altitude and inter-satellite range, n_r is estimated independently for every monthly solution and for each robust weighting realisation based on Tukey's bisquare scheme.

Each scatter point therefore represents a distinct combination of (i) a pair of initial orbital conditions, (ii) a monthly gravity-grid solution, and (iii) a specific robust weight configuration. This procedure yields a large ensemble of statistically independent estimates rather than repeated realisations of a single setup, intentionally sampling both physical variability in orbital geometry and methodological sensitivity arising from robust outlier treatment.

D.2 Quality metrics

The quality of each simulation realisation is evaluated using several complementary metrics. These metrics are computed independently for each estimate of n_r and are later used to assess the robustness and validity of the correction.

The following measures are considered:

- R^2 (time-series): the coefficient of determination obtained from a direct comparison between simulated and predicted time series;
- R^2 (grid): the coefficient of determination computed after gridding both simulated and predicted observables onto monthly $2^\circ \times 2^\circ$ spatial grids;
- RMSE: the root-mean-square error of the observable;
- Median Absolute Error Difference: defined as the median reduction in absolute error with respect to the uncorrected case, with positive values indicating improved agreement.

D.3 Distribution and interpretation of n_r

Fig. 22 illustrates the distribution of empirically estimated orbital radius exponents n_r together with their associated quality metrics for (**a**) LGD and (**b**) residual range. While both observables exhibit stable performance at the gridded level over a wide range of simulations, their sensitivity to orbital altitude and the resulting variability in n_r differ markedly.

For LGD (Fig. 22a), the inferred values of n_r span a relatively wide range, approximately from 10 to 21. This spread reflects the strong sensitivity of LGD to high-frequency gravity signals, for which variations in orbital altitude significantly modulate signal attenuation. Consequently, changes in altitude between simulation pairs (e.g. ∼200 km versus ∼700 km) lead to appreciable differences in the optimal scaling exponent. This variability manifests primarily in the time-series metric, where R^2 (time-series) highlights local temporal mismatches that are not always fully corrected by a single global exponent. Despite this sensitivity, the gridded performance remains robust. As shown on the horizontal axis of Fig. 22a, R^2 (grid) values concentrate strongly between 0.90 and 0.99, with a dominant peak near 0.95. Only a small number of cases exhibit substantially lower R^2 (grid) values (down to ∼0.5). This confirms that, although local temporal variations may not always be perfectly reproduced, the proposed correction effectively captures the dominant signal amplitudes that govern the gridded monthly grids relevant for mass-change estimation.

In contrast, residual range exhibits a much narrower distribution of orbital radius exponents (Fig. 22b), with most n_r values clustered between approximately 8 and 10. This behaviour is consistent with the analytical results presented in App. C, which predict a weak dependence of the residual range observable on orbital altitude. Residual range is dominated by low-frequency signals, whose attenuation with altitude is significantly smaller than that of the higher-frequency components governing LGD. As a result, variations in altitude introduce only minor changes in the effective scaling exponent. This reduced sensitivity is also reflected in the quality metrics. For residual range (Fig. 22b), R^2 (grid) values are tightly constrained between approximately 0.92 and 0.99, with substantially less spread than observed for LGD. The corresponding time-series R^2 values are likewise more uniform, indicating fewer local mismatches and a more homogeneous correction behaviour across simulation cases.

The ensemble, for LGD (Fig. 22a), exhibits a mean orbital radius exponent of approximately $\bar{n}_r \approx 15$, with substantially larger spread than observed for residual

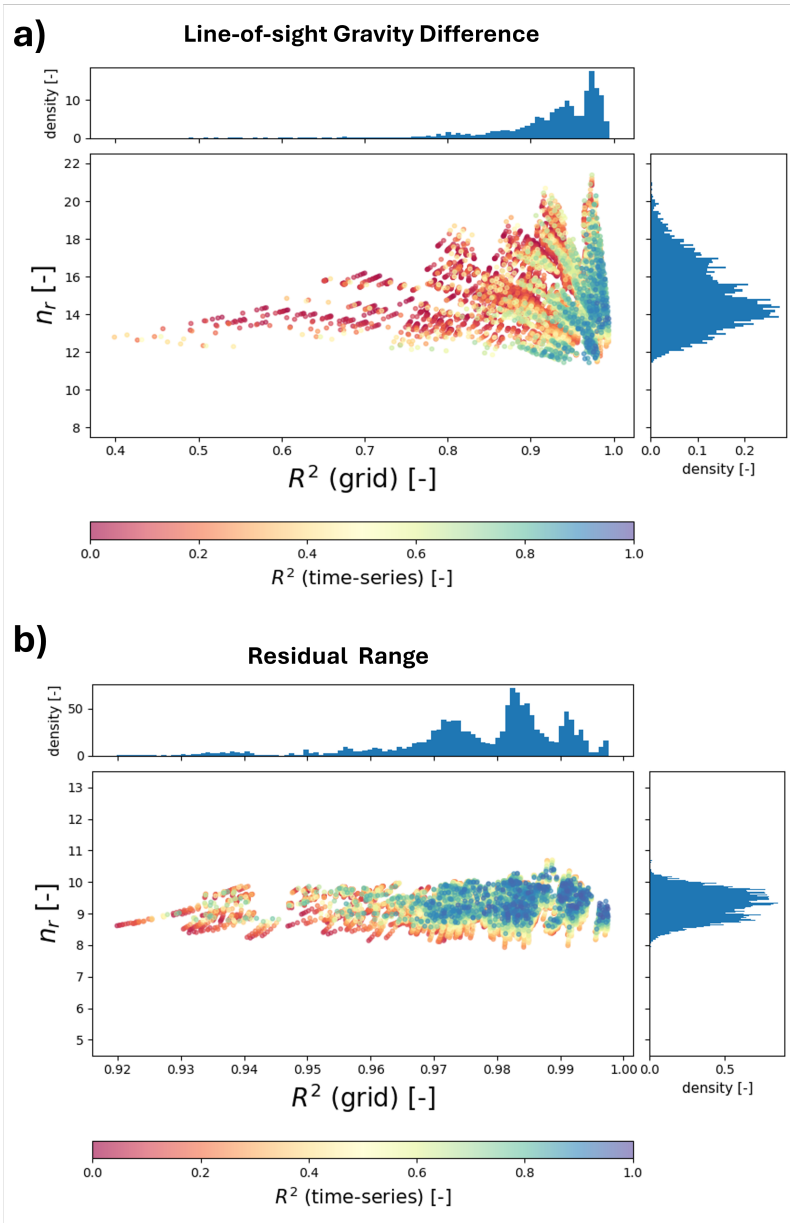


Fig. 22 Distribution of empirically estimated altitude power-law exponents n_r for (**a**) line-of-sight gravity difference (LGD) and (**b**) residual range across the full ensemble of simulations. Each point corresponds to one estimate of n_r derived from a combination of initial-condition pairs, monthly solution, and robust weighting realisation. Colours indicate the coefficient of determination at the time-series level (R^2 (time-series)). The horizontal axis shows the coefficient of determination after gridding onto monthly $2^\circ \times 2^\circ$ grids (R^2 (grid)), and the vertical axis denotes n_r. Marginal histograms show the distributions of R^2 (grid) and n_r.

range. This reflects the strong sensitivity of LGD to high-frequency gravity signals and, consequently, to orbital altitude variations. For residual range (Fig. 22b), the inferred exponents are much more tightly clustered, with a mean value of $\bar{n}_r \approx 9.3$ and a standard deviation of 0.45.

In both cases, however, the distributions are non-Gaussian and influenced by extreme simulation configurations that exceed the range of orbital variability realised during the GRACE mission. To ensure methodological consistency between observables and to limit sensitivity to such extremes, the representative global orbital radius exponents are therefore derived using the robust statistical framework for both LGD and residual range, namely the median and robust standard deviation (Eq. 15 and Eq. 16) described in Sect. 3.3. The resulting constant estimates adopted for subsequent analyses are summarised in Table 6.

D.4 Verification of the estimated exponent

The robustness of the constant exponent n_r is evaluated by reapplying the estimated global values to the full ensemble of synthetic simulations. Performance is assessed as a function of normalised altitude and inter-satellite range ratios, shown on logarithmic axes in Fig. 23, where each point represents a single simulation realisation. Due to the logarithmic scaling, nearby configurations are visually compressed, such that individual points may represent small clusters of seven tightly localised realisations. Results are shown for LGD (a) and residual range (b), each evaluated using three quality metrics: (i) R^2 (grid), (ii) RMSE, and (iii) Median Absolute Error Difference. The diagonal $y = x$ highlights cases where altitude and range vary simultaneously; along this line, compensating effects are strongest, and the constant-exponent approximation performs least well. For LGD, this is evidenced by increased RMSE values ranging from $\sim$1 to above 2.5 nm/s^2 (Fig. 23a(ii)), reduced R^2 spanning from below 0.75 up to 0.85 (Fig. 23a(i)), and limited or negative improvements (Fig. 23a(iii). For residual range, this behaviour is less pronounced in R^2, which remains within 0.92–0.99 (Fig. 23b(i)), although the lower values are still concentrated along the diagonal. In contrast, RMSE increases from approximately 5 to above 10 μm along this line (Fig. 23b(ii)), while improvements are minimal (of order $\sim$0.1 μm) or even negative (Fig. 23b(iii).

Away from the diagonal, the correction performs consistently well. In particular, in the case of constant altitude and varying inter-satellite range; R^2 reaches values between 0.95 and 0.99 for both LGD and residual range (Fig. 23a(i),b(i)). RMSE values remain low, on the order of $\sim$0.1–0.5 nm/s^2 for LGD and $\sim$1–5 μm for residual range (Fig. 23a(ii),b(ii)). Correspondingly, improvements are consistently positive, reaching $\sim$1.5 to above 2.5 nm/s^2 for LGD and $\sim$10 μm or more for residual range (Fig. 23a(iii),b(iii)). Along the constant-range axis, the behaviour is more complex due to the altitude dependence of n_r (App. C). In this case, improvements vary more broadly, ranging from approximately 0.25 to 2.5 nm/s^2 for LGD and $\sim$4 to 10 μm for residual range (Fig. 23a(iii),b(iii)).

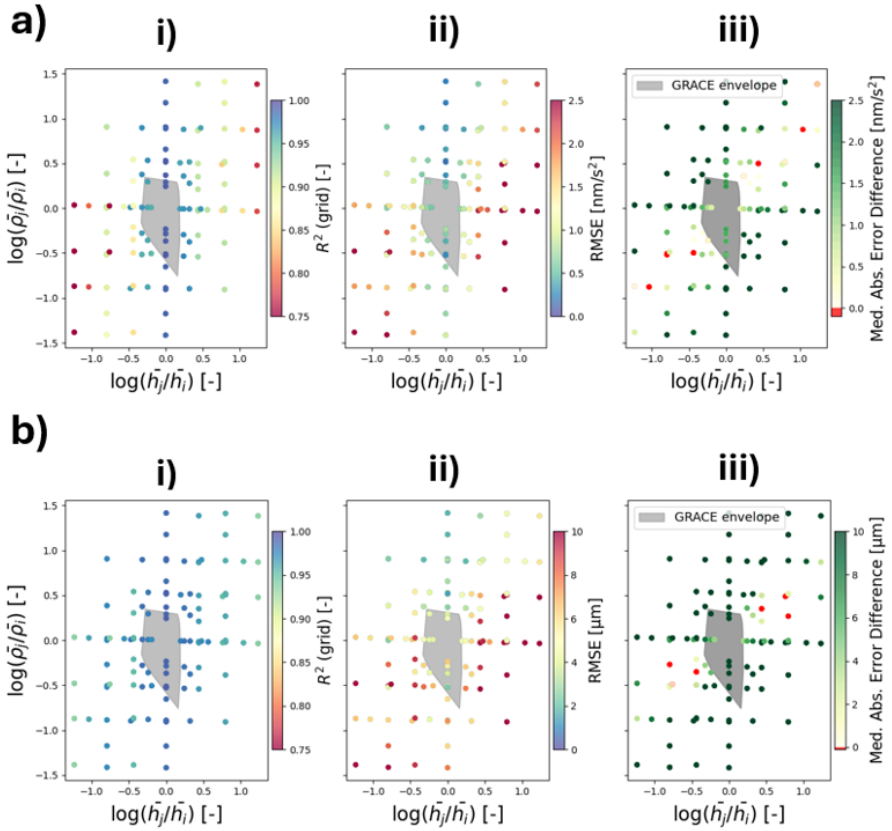


Fig. 23 Verification of the correction scheme within the GRACE operational envelope. (a) Results for LGD and (b) for residual range. For each observable, the panels (i)–(iii) show the spatial distributions of the quality metrics: (i) coefficient of determination R^2 (grid), (ii) root-mean-square error (RMSE) expressed in the native units of the observable (nm/s^2 for LGD and μm for range), and (iii) median absolute error difference.

To quantify the practical relevance, statistics are computed for simulations within the GRACE operational envelope, defined by the observed monthly extremes of altitude and range ratios over the mission lifetime. Table 8 shows that high agreement is achieved for both observables, with mean R^2 values of 0.985 (LGD) and 0.988 (range), and low RMSE levels (0.333 nm/s^2 for LGD and 2.634 μm for range). The Median Absolute Error Difference further indicates consistent error reduction across the ensemble. Quantitatively, the achieved improvements exceed the residual errors by a substantial margin: for LGD, the mean improvement (1.064 nm/s^2) is more than three times the mean RMSE (0.333 nm/s^2), and even exceeds the maximum RMSE (0.897 nm/s^2, ∼19% larger), while the maximum improvement (3.292 nm/s^2) is nearly four times the maximum RMSE. For residual range, the mean improvement (10.098 μm) is approximately four times the mean RMSE (2.634 μm), and exceeds the maximum RMSE (7.308 μm, ∼38% larger), with the maximum improvement (32.941 μm) being more than four times larger than the maximum RMSE (∼350%).

Table 8 Summary statistics of validation metrics for LGD and residual range within the GRACE operational envelope ($N = 77$).

Metric	Mean	Min	Max	Std
R^2 (grid)	0.985	0.956	0.997	0.013
RMSE (LGD, nm/s^2)	0.333	0.069	0.897	0.202
Median Absolute Error Difference (LGD, nm/s^2)	1.064	0.218	3.292	0.627
R^2 (range)	0.988	0.967	0.998	0.007
RMSE (range, μm)	2.634	0.484	7.308	1.621
Median Absolute Error Difference (range, μm)	10.098	1.432	32.941	6.711

Overall, these results demonstrate that within GRACE-like orbital conditions the constant-exponent correction consistently reduces residual errors, with improvements systematically exceeding the remaining variability across all configurations. This confirms the robustness of a single global orbital radius exponent for each observable and supports its use in subsequent mass-change retrievals.

References

Barthelmes F (n.d.) Low Pass Filtering of Gravity Field Models by Gently Cutting the Spherical Harmonic Coefficients of Higher Degrees. International Centre for Global Earth Models (ICGEM), GFZ German Research Centre for Geosciences, URL https://icgem.gfz-potsdam.de/docs/gentlecut_engl.pdf, accessed: 17 December 2025

Bettadpur S (2018a) GRACE Level-2 Processing Standards Document. Center for Space Research, The University of Texas at Austin, URL https://podaac-tools.jpl.nasa.gov/drive/files/allData/grace/docs/L2-CSR006_ProcStd_v5.0.pdf, rev 5.0 Apr 18, 2018, For Level-2 Product Release 0006

Bettadpur S (2018b) Gravity Recovery and Climate Experiment Level-2 Gravity Field Product User Handbook. Center for Space Research, The University of Texas at Austin, URL https://archive.podaac.earthdata.nasa.gov/podaac-ops-cumulus-docs/grace/open/docs/L2-UserHandbook_v4.0.pdf

Bettadpur S, Save H, Tapley B, et al (2025) CSR RL06 GRACE geofit and postfit dataset. https://doi.org/10.18738/T8/VY3U8L

Boergens E (2021) Python package regional tws uncertainty. https://doi.org/10.5880/GFZ.1.3.2021.005

Boergens E, Kvas A, Eicker A, et al (2022) Uncertainties of GRACE-Based Terrestrial Water Storage Anomalies for Arbitrary Averaging Regions. Journal of Geophysical Research: Solid Earth 127(2):e2021JB022081. https://doi.org/10.1029/2021JB022081

Bureau of Meteorology (2013) Tropical cyclone Oswald. URL http://www.bom.gov.au/cyclone/history/Oswald.shtml, accessed: 2024-11-01

Case K, Kruizinga G, Wu SC (2010) GRACE Level 1B Data Product User Handbook. URL https://podaac-tools.jpl.nasa.gov/drive/files/allData/grace/docs/Handbook_1B_v1.3.pdf

Chen Q, Shen Z, Sun Y, et al (2023) Tongji-GRACE2022: New global temporal earth's gravity field models derived from K-band and LRI inter-satellite range-rate data. In: XXVIII General Assembly of the International Union of Geodesy and Geophysics (IUGG), Berlin, Germany, https://doi.org/10.57757/IUGG23-0878

Cuadrat-Grzybowski M, Teixeira da Encarnacao JG, Visser PNAM (2025) Potential of Ka-Band Range Rate Post-Fit Residuals for High-Frequency Mass Change Applications. Journal of Geophysical Research: Solid Earth 130(12):e2025JB031615. https://doi.org/10.1029/2025JB031615

Cuadrat-Grzybowski M, Visser P, De Teixeira da Encarnacao J (2026a) TUD-L3-EWH_UNC-GRACE: A Global Level-3 GRACE(-FO) EWH Uncertainty Product. EarthArXiv Preprint, https://doi.org/10.31223/X5V19X

Cuadrat-Grzybowski M, Visser P, Jacobs F, et al (2026b) TUD-L3Uncorr-5dayEWH-GRACEv2: Novel and Global 0.5°x0.5° 5-day GRACE equivalent water height gridded product. 4TU.ResearchData, https://doi.org/10.4121/a685e7cf-1b84-4007-b206-89ae1c71dd6c.v2

Dahle C, Murböck M, Flechtner F, et al (2019) The GFZ GRACE RL06 Monthly Gravity Field Time Series: Processing Details and Quality Assessment. Remote Sensing 11(18). https://doi.org/10.3390/rs11182116

Deng D, Ritchie EA (2020) Rainfall Mechanisms for One of the Wettest Tropical Cyclones on Record in Australia—Oswald (2013). Monthly Weather Review 148(6):2503 – 2525. https://doi.org/10.1175/MWR-D-19-0168.1

Dirkx D, Fayolle M, Garrett G, et al (2022) The open-source astrodynamics Tudatpy software – overview for planetary mission design and science analysis. In: Europlanet Science Congress 2022, Granada, Spain, pp EPSC2022–253, https://doi.org/10.5194/epsc2022-253

Frappart F, Ramillien G, Seoane L (2016) Monitoring Water Mass Redistributions on Land and Polar Ice Sheets Using the GRACE Gravimetry from Space Mission. Land Surface Remote Sensing in Continental Hydrology pp 255–279. https://doi.org/10.1016/B978-1-78548-104-8.50008-5

Ghobadi-Far K, Han SC, Weller S, et al (2018) A Transfer Function Between Line-of-Sight Gravity Difference and GRACE Intersatellite Ranging Data and an Application to Hydrological Surface Mass Variation. Journal of Geophysical Research: Solid Earth 123:9186–9201. https://doi.org/10.1029/2018JB016088

Ghobadi-Far K, Han SC, Allgeyer S, et al (2020) GRACE gravitational measurements of tsunamis after the 2004, 2010, and 2011 great earthquakes. Journal of Geodesy 94:1–9. https://doi.org/10.1007/S00190-020-01395-3

Ghobadi-Far K, Han SC, McCullough CM, et al (2022) Along-orbit analysis of GRACE Follow-On inter-satellite Laser Ranging Measurements for sub-monthly surface mass variations. Journal of Geophysical Research: Solid Earth 127. https://doi.org/10.1029/2021JB022983

Gouweleeuw BT, Kvas A, Gruber C, et al (2018) Daily GRACE gravity field solutions track major flood events in the Ganges–Brahmaputra Delta. Hydrology and Earth System Sciences 22:2867–2880. https://doi.org/10.5194/hess-22-2867-2018

Güntner A, Sharifi E, Haas J, et al (2024) Global Gravity-based Groundwater Product (G3P) (Version 1.12). GFZ Data Services, https://doi.org/10.5880/G3P.2024.001

Han SC, Sauber J, Luthcke S (2010) Regional gravity decrease after the 2010 Maule (Chile) earthquake indicates large-scale mass redistribution. Geophysical Research Letters 37(23). https://doi.org/10.1029/2010GL045449

Han SC, Ghobadi-Far K, Yeo IY, et al (2021a) GRACE Follow-On revealed Bangladesh was flooded early in the 2020 monsoon season due to premature soil saturation. Proceedings of the National Academy of Sciences 118(47):e2109086118. https://doi.org/10.1073/pnas.2109086118

Han SC, Yeo IY, Khaki M, et al (2021b) Novel along-track processing of GRACE Follow-On laser ranging measurements found abrupt water storage increase and land subsidence during the 2021 March Australian flooding. Earth Space Sci 8(11). https://doi.org/10.1029/2021EA001941

Ince ES, Barthelmes F, Reißland S, et al (2019) ICGEM – 15 years of successful collection and distribution of global gravitational models, associated services, and future plans. Earth Syst Sci Data 11(2):647–674. https://doi.org/10.5194/essd-11-647-2019

Islam AS, Haque A, Bala SK (2010) Hydrologic characteristics of floods in Ganges–Brahmaputra–Meghna (GBM) delta. Natural Hazards 54:797–811. https://doi.org/10.1007/s11069-010-9504-y

Jäggi A, Meyer U, Lasser M, et al (2022) International combination service for time-variable gravity fields (COST-G). In: Freymueller JT, Sánchez L (eds) Beyond 100: The Next Century in Geodesy. Springer International Publishing, Cham, pp 57–65, https://doi.org/10.1007/1345_2020_109

Kim J (2000) Simulation Study of A Low-Low Satellite-to-Satellite Tracking Mission. Phd dissertation, The University of Texas at Austin, https://doi.org/10.26153/tsw/12695

Kurtenbach E, Eicker A, Mayer-Gürr T, et al (2012) Improved daily GRACE gravity field solutions using a Kalman smoother. Journal of Geodynamics 59-60:39–48. https://doi.org/10.1016/j.jog.2012.02.006

Kusche J, Schmidt R, Petrovic S, et al (2009) Decorrelated GRACE time-variable gravity solutions by GFZ, and their validation using a hydrological model. Journal of Geodesy 83:903–913. https://doi.org/10.1007/s00190-009-0308-3

Kvas A (2018) l3py software. Zenodo, https://doi.org/10.5281/zenodo.1450899

Kvas A, Behzadpour S, Ellmer M, et al (2019) ITSG-Grace2018: Overview and evaluation of a new GRACE-only gravity field time series. Journal of Geophysical Research: Solid Earth 124:9332–9344. https://doi.org/10.1029/2019JB017415

Lemoine JM, Bourgogne S (2020) RL05 monthly and 10-day gravity field solutions from CNES/GRGS. In: GSTM2020-51, https://doi.org/10.5194/gstm2020-51

Lemoine JM, Bruinsma S, Loyer S, et al (2007) Temporal gravity field models inferred from GRACE data. Advances in Space Research 39:1620–1629. https://doi.org/10.1016/j.asr.2007.03.062

Li F, Springer A, Kusche J, et al (2025a) Reanalysis and Forecasting of Total Water Storage and Hydrological States by Combining Machine Learning With CLM Model Simulations and GRACE Data Assimilation. Water Resources Research 61(2). https://doi.org/10.1029/2024WR037926

Li Hs, Yi S, Luo Zr, et al (2024) Revealing High-Temporal-Resolution Flood Evolution With Low Latency Using GRACE Follow-On Ranging Data. Water Resources Research 60(6):e2023WR036332. https://doi.org/10.1029/2023WR036332

Li Hs, Yi S, Han SC, et al (2025b) Daily Regional Gravity Field Estimation Using GRACE Follow-On Line-of-Sight Gravity Differences. Journal of Geophysical Research: Solid Earth 130(5):e2024JB030089. https://doi.org/10.1029/2024JB030089

Li Hs, Yi S, Tang H (2025c) Tracking Hurricane-Induced Water Storage Changes Using GRACE and GRACE-FO Measurements. Geophysical Research Letters 52(20):e2025GL116973. https://doi.org/10.1029/2025GL116973

Mayer-Gürr T, Behzadpur S, Ellmer M, et al (2018) ITSG-Grace2018 - monthly, daily and static gravity field solutions from GRACE. https://doi.org/10.5880/ICGEM.2018.003

McGirr R, Tregoning P, Allgeyer S, et al (2023) Interplay of Altitude, Ground Track Coverage, Noise, and Regularization in the Spatial Resolution of GRACE Gravity Field Models. Journal of Geophysical Research: Solid Earth 128(1):e2022JB024330. https://doi.org/10.1029/2022JB024330

Müller V (2017) Design considerations for future geodesy missions and for space laser interferometry. Doctoral thesis, Gottfried Wilhelm Leibniz University Hannover, https://doi.org/10.15488/9029

Peidou A, Landerer F, Wiese D, et al (2022) Spatiotemporal Characterization of Geophysical Signal Detection Capabilities of GRACE-FO. Geophysical Research Letters 49. https://doi.org/10.1029/2021GL095157

Pini AJ (2012) Investigation of the effect of repeat orbits on GRACE gravity recovery. Master's thesis, University of Texas-Austin, URL http://hdl.handle.net/2152/19704

Qian N, Chang G, Ditmar P, et al (2022) Sparse DDK: A Data-Driven Decorrelation Filter for GRACE Level-2 Products. Remote Sensing 14(12). https://doi.org/10.3390/rs14122810

Ramillien G, Frappart F, Seoane L (2016) Space Gravimetry Using GRACE Satellite Mission: Basic Concepts. Microwave Remote Sensing of Land Surfaces: Techniques and Methods pp 285–302. https://doi.org/10.1016/B978-1-78548-159-8.50006-2

Ramillien G, Seoane L, Schumacher M, et al (2020) Recovery of Rapid Water Mass Changes (RWMC) by Kalman Filtering of GRACE Observations. Remote Sensing 12(8). https://doi.org/10.3390/rs12081299

Rateb A, Save H, Sun AY, et al (2024) Rapid mapping of global flood precursors and impacts using novel five-day GRACE solutions. Scientific Reports 14:13841. https://doi.org/10.1038/s41598-024-64491-w

Ray RD, Luthcke SB, Boy J (2009) Qualitative comparisons of global ocean tide models by analysis of intersatellite ranging data. Journal of Geophysical Research: Oceans 114. https://doi.org/10.1029/2009JC005362

Retegui-Schiettekatte L, Schumacher M, Madsen H, et al (2025) Assessing daily GRACE Data Assimilation during flood events of the Brahmaputra River Basin. Science of The Total Environment 975:179181. https://doi.org/10.1016/j.scitotenv.2025.179181

Ries J, Bettadpur S, Eanes R, et al (2016) The Combined Gravity Model GGM05C. https://doi.org/10.5880/icgem.2016.002

Save H, Bettadpur S, Tapley BD (2016) High-resolution CSR GRACE RL05 mascons. Journal of Geophysical Research: Solid Earth 121(10):7547–7569. https://doi.org/10.1002/2016JB013007

Schindelegger M, Harker AA, Ponte RM, et al (2021) Convergence of Daily GRACE solutions and models of submonthly ocean bottom pressure variability. Journal of Geophysical Research: Oceans 126. https://doi.org/10.1029/2020JC017031

Schmidt R, Flechtner F, Meyer U, et al (2008) Hydrological signals observed by the GRACE satellites. Surv Geophys 29(4-5):319–334. https://doi.org/10.1007/s10712-008-9033-3

Spero R (2021) Point-mass sensitivity of gravimetric satellites. Advances in Space Research 67(5):1656–1664. https://doi.org/10.1016/j.asr.2020.12.019

Sun AY, Save H, Rateb A, et al (2024) Deciphering the role of total water storage anomalies in mediating regional flooding. Geophysical Research Letters 51. https://doi.org/10.1029/2023GL108126

Wahr J (2015) Time-Variable Gravity from Satellites. In: Schubert G (ed) Treatise on Geophysics (Second Edition), second edition edn. Elsevier, Oxford, p 193–213, https://doi.org/10.1016/B978-0-444-53802-4.00065-8

Weigelt M (2017) The acceleration approach. In: Naeimi M, Flury J (eds) Global gravity field modeling from satellite-to-satellite tracking data, Lecture Notes in Earth System Sciences. Springer International Publishing, Cham, Switzerland, p 127–160

Werth S, Güntner A, Schmidt R, et al (2009) Evaluation of GRACE filter tools from a hydrological perspective. Geophysical Journal International 179(3):1499–1515. https://doi.org/10.1111/j.1365-246X.2009.04355.x

Wiese DN, Landerer FW, Watkins MM (2016) Quantifying and reducing leakage errors in the JPL RL05M GRACE mascon solution. Water Resources Research 52(9):7490–7502. https://doi.org/10.1002/2016WR019344

Wouters B, Gardner AS, Moholdt G (2019) Global glacier mass loss during the GRACE satellite mission (2002-2016). Frontiers in Earth Science 7. https://doi.org/10.3389/feart.2019.00096

Wu WY, Yang ZL, Zhao L, et al (2022) The impact of multi-sensor land data assimilation on river discharge estimation. Remote Sensing of Environment 279:113138. https://doi.org/10.1016/j.rse.2022.113138

Xiong Y, Feng W, Zhou X, et al (2024) Separation of earthquake and hydrology signals from GRACE satellites data via independent component analysis: a case study in the Sumatra region. Geophysical Journal International 239(3):1597–1616. https://doi.org/10.1093/gji/ggae351

Yang F, Schumacher M, Retegui-Schiettekatte L, et al (2025) PyGLDA: a fine-scale python-based global land data assimilation system for integrating satellite gravity data into hydrological models. Geoscientific Model Development 18(18):6195–6217. https://doi.org/10.5194/gmd-18-6195-2025

Yuan D (2018) Gravity Recovery and Climate Experiment: JPL Level-2 Processing Standards Document for Level-2 Product Release 06. Technical report, Jet Propulsion Laboratory, California Institute of Technology, URL https://icgem.gfz-potsdam.de/docs/GRACE_JPL_L2_Processing_Standards_Document_for_RL06.pdf, jPL 327-744 (v 6.0)

Zhang L, Shen Y, Ji K, et al (2024) Covariance Matrix Reconstruction of GRACE Monthly Solutions Using Common Factors and Individual Formal Errors. IEEE Journal of Selected Topics in Applied Earth Observations and Remote Sensing 17:15567–15582. https://doi.org/10.1109/JSTARS.2024.3405560

Zhou H, Zheng L, Li Y, et al (2024) HUST-Grace2024: a new GRACE-only gravity field time series based on more than 20 years of satellite geodesy data and a hybrid processing chain. Earth System Science Data 16(7):3261–3281. https://doi.org/10.5194/essd-16-3261-2024

Zhu Z, Wang C, Yan Y, et al (2025) Assessing the Performance of GRACE-FO KBR and LRI in Detecting Mass Changes Using Along-Orbit Range-Accelerations. Journal of Geophysical Research: Solid Earth 130(6):e2024JB029428. https://doi.org/10.1029/2024JB029428